

Spring 1995

Dynamics of Dipoles in the Middle Atlantic Bight

Bruce L. Lipphardt Jr.
Old Dominion University

Follow this and additional works at: https://digitalcommons.odu.edu/oeas_etds



Part of the [Atmospheric Sciences Commons](#), and the [Oceanography Commons](#)

Recommended Citation

Lipphardt, Bruce L.. "Dynamics of Dipoles in the Middle Atlantic Bight" (1995). Doctor of Philosophy (PhD), Dissertation, Ocean & Earth Sciences, Old Dominion University, DOI: 10.25777/0byc-t184
https://digitalcommons.odu.edu/oeas_etds/50

This Dissertation is brought to you for free and open access by the Ocean & Earth Sciences at ODU Digital Commons. It has been accepted for inclusion in OES Theses and Dissertations by an authorized administrator of ODU Digital Commons. For more information, please contact digitalcommons@odu.edu.

DYNAMICS OF DIPOLES IN THE MIDDLE ATLANTIC BIGHT

by

Bruce L. Lipphardt, Jr.

Bachelor of Science, Oceanography, 1984
U. S. Naval Academy, Annapolis, Maryland

A Dissertation submitted to the Faculty of
Old Dominion University in Partial Fulfillment of the
Requirements for the Degree of

Doctor of Philosophy

Oceanography

Old Dominion University
March, 1995

Approved by:

Dr. A. D. Kirwan, Jr. (chairman)

Dr. [✓]John Adam

Dr. ~~Stanford~~ B. Hooker

~~Dr.~~ John Klinck

Dr. Richard P. Mied

Abstract

DYNAMICS OF DIPOLES IN THE MIDDLE ATLANTIC BIGHT

Bruce L. Lipphardt, Jr.

Old Dominion University, 1995
Advisor: Dr. A. D. Kirwan, Jr.

Beginning with the observations made by the Warm-Core Rings program in the early 1980's, several Gulf Stream warm-core rings (WCR's) in the Middle Atlantic Bight (MAB) have been observed with one or more cyclones around their periphery. These *ring systems* are observed in the slope water between the Gulf Stream's western boundary and the shelf break. Observations of ring systems have motivated a reanalysis of existing satellite surface temperature imagery, which revealed that multipole structure is common for both warm and cold core rings. This suggests that rings are better characterized as one part of multipole systems rather than as isolated vortices.

Dynamical studies of ring systems have been primarily limited to numerical modeling of isolated nonlinear vortices and interactions of vortices with sloping topography. Here, a baroclinic rotating modon model is used to simulate the dynamics of a WCR paired with a peripheral cyclone, over a flat bottom. Observations of WCR 82B and a peripheral cyclone are used to constrain the model parameters.

A diagnostic calculation compares model ring and cyclone velocity profiles with observations and provides estimates of ring and dipole energies, as well as an estimate of volume transport across a 150 km section representing the MAB shelf-slope front. In addition, four different methods for estimating the location of the ring and cyclone perimeters are compared.

Results are also presented for two evolutionary calculations. The first calculation uses three groups of fluid parcels, allowed to evolve for 14 days, to simulate three flow features apparent in satellite imagery of the WCR 82B system. The second calculation simulates entrainment of shelf water and Gulf Stream water by allowing two long, thin patches of fluid parcels to evolve for 7.4 days. The final parcel distribution is again compared with satellite imagery for the WCR 82B system.

These results show that the rotating baroclinic modon model provides a useful dynamical simulation of a dipolar ring system. The model produces a velocity field that is consistent with observations, and it allows ring and dipole energies, volume transport, and ring and cyclone perimeter position to be estimated.

This work is dedicated to Denny Kirwan, who both encouraged and inspired me to seek a graduate degree, and, after describing the mentor–protegé relationship to me, has become the ideal mentor.

Acknowledgments

This research was supported by the Department of Defense National Defense Science and Engineering Graduate Fellowship program, and by the Office of Naval Research under contract N00014-91-J-1560.

All of the imagery shown was processed at RSMAS, University of Miami, using the DSP software package developed by Otis Brown and Robert Evans.

I am grateful to Dr. Denny Kirwan for his support and encouragement throughout my tenure as his student. I am also thankful to all of the members of the Center for Coastal Physical Oceanography faculty, who have provided guidance and encouragement whenever needed. I am especially thankful to my dissertation committee members, Dr. John Adam, Dr. Stan Hooker, Dr. John Klinck, and Dr. Richard Mied, for all of their personal encouragement and technical advice.

Finally, this work could not have been done without the love and support of my parents, and my three sisters and their families. I am especially grateful to Carole, who has endured my endless frustration and anxiety and has always been at my side with a smile to tell me that I could do it.

Contents

1	Introduction	1
1.1	Circulation on the Middle Atlantic Bight Shelf	1
1.2	Shelf-Slope Exchange Processes in the MAB	1
1.3	WCR's in the Middle Atlantic Bight	2
1.4	Observations of Ring Systems in the MAB Shelf-Slope Region	4
1.5	Modeling the Dynamics of Ring Systems	7
1.6	Overview of This Research	9
2	Research Questions	13
3	Description of the Baroclinic Modon Model	15
3.1	Introduction	15
3.2	The Rotating Baroclinic Modon Model	15
3.3	Solutions	22
4	Sensitivity of the Model to Parameter Changes	27
4.1	Background	27
4.2	Choosing the Environmental Parameters	28
4.3	The Geometric Parameters	29
4.4	The Lower Layer Rider Amplitude	29
4.5	Evaluating the Model's Sensitivity	30
4.6	Results of Model Sensitivity Study	33
4.7	Summary	38
5	Simulating the WCR 82B System as a Modon	41
5.1	Introduction	41
5.2	Results of the Diagnostic Calculation	42
5.2.1	Upper Layer Kinematics	42

5.2.2	Locating the Ring and Cyclone Perimeters	50
5.2.3	Upper Layer Energetics	56
5.2.4	Upper Layer Volume Transport	57
5.2.5	Lower Layer Kinematics	60
5.3	Results of the Evolutionary Calculations	62
6	Discussion and Conclusions	73
6.1	Limitations of the Modon Model	73
6.2	Discussion of Results	76
6.3	Conclusions	79
6.4	What's the Next Step?	80

List of Tables

1	Summary of baroclinic modon model parameters	26
2	Observations of WCR 82B system used for evaluating sensitivity study	31
3	Parameter sets used for model sensitivity study	33
4	Parameter values used to simulate the WCR 82B system	40

List of Figures

1	Map of the Middle Atlantic Bight region, showing the locations of warm-core rings studied by the Warm-Core Rings program during 1981–1982.	5
2	The physical setting for the baroclinic modon model.	17
3	E_{min} versus \hat{r}_2 for the first 12 parameter sets in the sensitivity study.	35
4	Peak relative vorticities and ring energies versus \hat{r}_2 for the first 12 parameter sets in the sensitivity study.	37
5	Contours of $\hat{\psi}_1$ field and upper layer velocity vectors for the diagnostic calculation.	43
6	East–west velocity versus distance from the origin along the line between the cyclone and ring centers.	45
7	Observed and modeled profiles of ring radial and azimuthal velocity.	46
8	Observed and modeled profiles of cyclone radial and azimuthal velocity.	48
9	Contours of \hat{q}_1 and \hat{T}_1 for the diagnostic calculation.	51
10	Four different methods for estimating ring and cyclone perimeters.	54
11	Volume transport through a north–south section representing the MAB shelf–slope front.	59
12	Contours of $\hat{\psi}_2$ field and lower layer velocity vectors for the diagnostic calculation.	61
13	Contours of \hat{q}_2 and \hat{T}_2 for the diagnostic calculation.	63
14	Initial conditions for the two evolutionary calculations.	66
15	Comparison of 24 April 1982 surface temperature image with parcel distributions from the first evolutionary calculation after 14 days.	68
16	Comparison of 23 April 1982 surface temperature image with parcel distributions from the second evolutionary calculation after 7.4 days.	70

1 Introduction

1.1 Circulation on the Middle Atlantic Bight Shelf

The Middle Atlantic Bight (MAB) is the portion of the eastern U. S. continental shelf that extends southward from Cape Cod to Cape Hatteras. This region is about 800 km long, with a typical shelf width of 100 km. The shelf is widest (about 150 km) adjacent to Long Island and narrowest (about 50 km) at Cape Hatteras. The mean circulation on the shelf is well understood and is generally directed along-shelf, toward the southwest (Bumpus, 1973; Beardsley *et al.*, 1976; Beardsley and Boicourt, 1981; Allen *et al.*, 1983; Beardsley *et al.*, 1985). Recently, ^{18}O concentration data has been used to suggest a buoyancy driven coastal flow originating from glacial melt and runoff around southern Greenland and continuing southward along the Scotian Shelf and finally through the MAB (Chapman *et al.*, 1986; Chapman and Beardsley, 1989).

1.2 Shelf–Slope Exchange Processes in the MAB

The relatively cool, fresh MAB shelf water is separated from the warmer, more saline slope water by a sharp frontal zone called the shelf–slope front (Wright, 1976). This front spans the entire MAB shelf from Georges Bank to Cape Hatteras and is generally found near the 80 m isobath. Brink (1987) stated that the front's position can vary dramatically from day to day, and Houghton and Marra (1983) described frequent exchange of small (20 km or less in width) parcels of water across the front. Houghton *et al.* (1986) and Garvine *et al.* (1988) described small (on the order of 10 km in diameter), energetic shelfbreak eddies present near the shelf–slope front.

Observed increases in salinity and oxygen isotope ratio on the MAB shelf in the

direction of the alongshelf flow provide convincing evidence of exchange across the shelf-slope front (Ketchum and Keen, 1955; Wright, 1976; Fairbanks, 1982; Chapman *et al.*, 1986). Quantifying this exchange and understanding the dynamics of exchange processes is important for closing heat and salt budgets for the MAB shelf. Understanding such exchange is also a concern for biological studies of the highly productive shelf ecosystem, where nutrient budgets play an important role. Additionally, prediction of shelf flow to determine the fate of spilled oil or pollutants requires an understanding of cross-shelf exchange dynamics.

Four important shelf-slope exchange mechanisms have been identified through observations. Fine-scale interleaving at the shelf-slope front results in mass exchange from turbulence and double diffusion (Voorhis *et al.*, 1976). At larger scales, thin lenses of shelf water, 10–20 km in diameter, have been observed to “calve off” and detach into the slope water (Wright, 1976). Garvine *et al.* (1988) described the morphology of small eddies, with diameters up to 40 km, located at the shelf-slope front, associated with plumes of MAB shelf water extending out into the slope region. Finally, at the largest scales, interactions of warm-core rings (WCR’s) with the shelf-slope front have been frequently observed, and exchange of shelf and slope water is readily apparent in satellite images of surface temperature taken during such interactions.

1.3 WCR’s in the Middle Atlantic Bight

WCR’s are formed when a northward meander of the Gulf Stream pinches off in the slope water region between the MAB shelf and the Gulf Stream (Saunders, 1971; Gotthardt and Potocsky, 1974). They consist of a core of warmer Sargasso Sea water surrounded by anticyclonically circulating Gulf Stream water. They are typically 100 km in diameter, and they tend to move west (southwest along the MAB shelf break) at mean speeds of about 0.05 m s^{-1} (Richardson, 1983). Typically,

about five WCR's form per year (Lai and Richardson, 1977; Richardson *et al.*, 1978; Richardson, 1983). Brown *et al.* (1986) examined the statistical properties of 10 years of WCR observations, including 87 individual rings. Their study showed a bimodal distribution of WCR lifetimes, with a short-lived mean of 54 days, and a long-lived mean of 229 days.

There are numerous observations of WCR interactions with shelf water prior to 1980, both in the MAB (Saunders, 1971; Morgan and Bishop, 1977; Mooers *et al.*, 1979; Fischer, 1980; Bisagni (1983); Ramp *et al.*, 1983; Beardsley *et al.*, 1985), and off Georges Bank (Smith, 1978; Fornshell and Criess, 1979). Halliwell and Mooers (1979) examined satellite derived surface temperature data for the shelf-slope front in the MAB between September 1975 and September 1977. During this period, 14 WCR's were observed, about half of which interacted noticeably with the shelf. Joyce *et al.* (1992) provided an excellent discussion of existing estimates of the frequency of occurrence of entrainment of MAB shelf water by WCR's. They estimated that 0.3–2 effective rings per year drive cross-shelf exchange at the MAB shelf break.

Beginning with the observations made by the Warm-Core Rings program, more detailed observations of WCR's, including interactions of WCR's with MAB shelf water, have been made since 1980. Evans *et al.* (1985) provided a detailed chronology of the life of WCR 82B as part of the Warm-Core Rings program. WCR 82B was tracked from its formation in early February 1982 until it collided with the Gulf Stream in July 1982. During its lifetime, WCR 82B moved southwestward close to the MAB shelf break and was frequently observed to entrain shelf water and move it out onto the slope. Additionally, several small cyclones were observed at various times along the periphery of WCR 82B, resulting in more complex interactions with the shelf. Joyce *et al.* (1992) used hydrographic data and acoustic doppler current profiles to estimate a total volume transport for a streamer of MAB shelf water east of WCR 82B. They noted that the shelf water, once it is moved onto the slope, was

entrained by the Gulf Stream rather than wrapped around the ring and returned toward the shelf. Figure 1, taken from Joyce (1985), shows a map of the MAB region with the locations of some of the WCR's observed as part of the Warm-Core Rings program.

1.4 Observations of Ring Systems in the MAB Shelf-Slope Region

The observations just described clearly show that WCR's are an important part of the mesoscale dynamics in the MAB. However, recently, several authors suggest that these rings are *not* simple isolated structures, but in fact may have one or more oppositely signed peripheral vortices (Hooker and Brown, 1994; Hooker *et al.*, submitted manuscript), so that they should more properly be considered as part of a dynamically linked *ring system*.

Perhaps the most detailed observations of a ring system in the MAB were reported by Kennelly *et al.* (1985) as part of the Warm Core Rings program's study of WCR 82B. Several small cyclones, with diameters of 30–40 km, were observed around the perimeter of WCR 82B. Some of these cyclones persisted for a period of a few weeks. Two cyclones were observed to form to the northeast of WCR 82B and were advected anticyclonically around the ring's center. Increased transport of shelf water to the slope region accompanied both of these cyclone formation and advection events. Maximum velocities of $0.6\text{--}0.7\text{ m s}^{-1}$ were observed in the cyclones. The authors could not determine whether the cyclones were dynamically linked to the WCR, but they noted that modon theory might provide a dynamical framework for interpreting the combined circulation of the cyclone–anticyclone system.

Hooker and Brown (1994) reanalyzed many of the observations of WCR 82B and one of its peripheral cyclones to determine if they could be interpreted as an evolving dipole. They showed that WCR 82B was fundamentally a dipole structure for much of its eight month lifetime, with one cyclone evident intermittently in satellite images

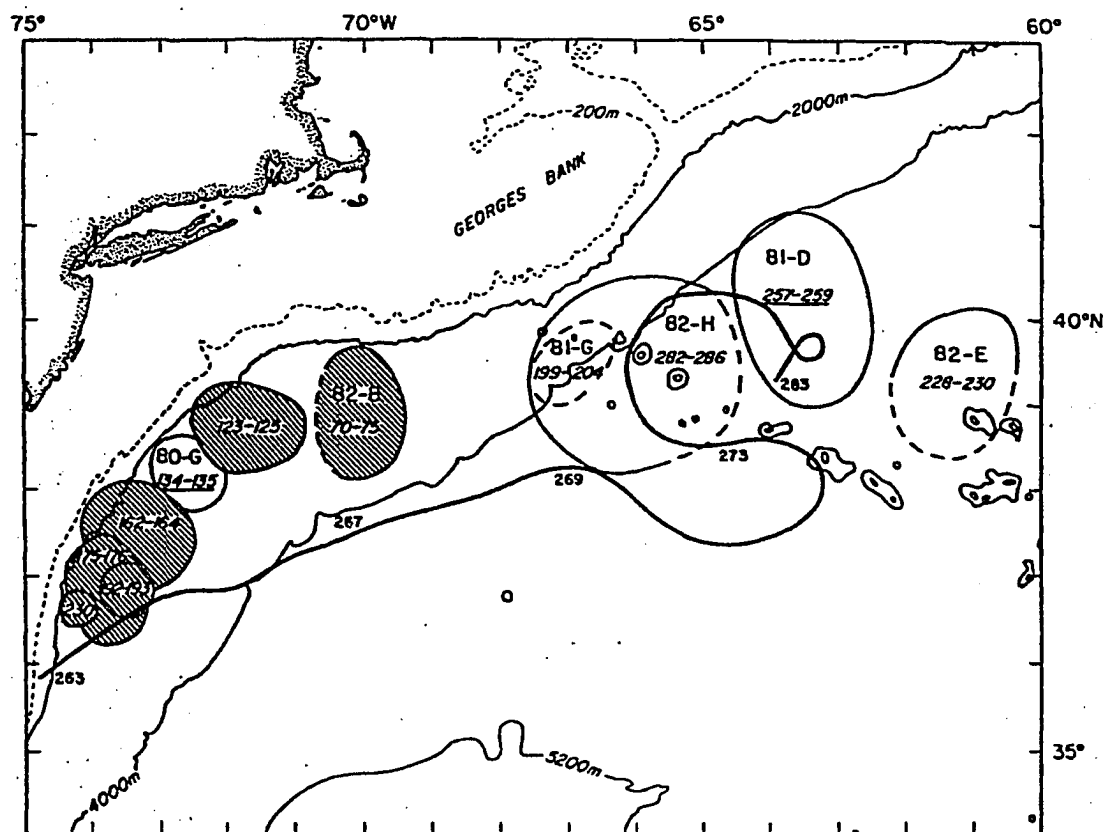


Figure 1: Map of the Middle Atlantic Bight region, showing the locations of warm-core rings studied by the Warm-Core Rings Program during 1981-1982. The sequential days of the year are shown, with 1981 dates underlined. Taken from Joyce (1985).

for a five week period as it rotated anticyclonically around the ring's center. The rotation period of the cyclone about the ring was estimated to be 25 days. Hooker and Brown (1994) also found dipolar structure in several satellite images of WCR 81F, which moved along the MAB shelf break just ahead of WCR 82B.

Earlier observations also suggested that cyclones might be paired with a WCR. Observations of WCR 81D reported by Joyce (1984) described a small cyclone to the northeast of the WCR's center, while the ring was located east of the New England Seamounts in 4500 m of water. Velocities of $0.10\text{--}0.15\text{ m s}^{-1}$ were observed in the cyclone, but no attempt was made to describe its size or shape.

In October 1983, Churchill *et al.* (1986) observed the passage of WCR 83D through a linear array of moored conductivity, temperature, and velocity sensors oriented across the MAB shelf as part of the Shelf Edge Exchange Processes (SEEP) program. WCR 83D was preceded through the array by a large (diameter about 80 km) cold-core cyclone with velocities less than 0.2 m s^{-1} . Surface slope water was observed moving onshore, and near bottom shelf water was observed moving offshore and around WCR 83D, suggesting that this ring-shelf interaction was a baroclinic event. The shoreward edge of the vortex pair appeared to closely follow the 2000 m isobath along the shelf slope, and there was no evidence of advection of the cyclone relative to the center of WCR 83D. The authors noted that this vortex pair resembled the modons observed in laboratory experiments (Flierl *et al.*, 1983), but no attempt was made to interpret these observations in terms of modon theory.

It is striking that ring systems were observed in the MAB in three consecutive years, 1981–1983. This implies that these systems occur frequently, often associated with interactions along the shelf-slope front. Examination of satellite surface temperature images often suggests the presence of coherent cyclonic features near WCR's. An example is the image shown by Fischer (1980), which contains two WCR's. The image shows a coherent cyclonic feature to the east of the northern WCR, with trans-

port of shelf water to the slope region evident in the area between the WCR and the cyclone. It is important to note that cyclonic features can be masked by heating of the surface layer and may not always be detectable by satellite measurements of surface temperature.

Frequent observations of WCR's, as part of ring systems, has motivated a reanalysis of existing satellite surface temperature imagery to determine whether multipole structure might be a common characteristic of both WCR's and cold-core rings (CCR's). Several examples of both WCR's and CCR's, as part of multipole ring groups, have been identified (S. Hooker, personal communication) both over the deep ocean and adjacent to the MAB shelf.

Although ring systems are often observed in the MAB, their dynamics are not well understood. Existing observations are not detailed enough to reveal how the individual vortices in a system are dynamically related. Understanding ring system dynamics is important in order to assess their role in cross-shelf transport and in the mesoscale energy budget. Once their dynamics are better understood, their effects can be properly accounted for in regional and general circulation models.

1.5 Modeling the Dynamics of Ring Systems

Recurring observations of ring systems in the MAB raise an important question about their dynamics and motivate a radical departure from existing ring models:

- *What if Gulf Stream rings are not isolated features, but are actually multipole vortices?*

Many different dynamical models for isolated WCR's have been proposed. Some examples are: Flierl (1979), Nof (1981), Kirwan *et al.* (1984), Nof (1985), and Cushman-Roisin *et al.* (1985). However, less attention has been paid to modeling the dynamics of ring systems. Smith and O'Brien (1983) used a two-layer primitive

equation model to study the interaction of mesoscale rings with a western bounding topographic slope. They showed that anticyclones of sufficient strength evolved into eastward propagating vortex pairs, with a cyclone developing as a result of the anticyclone-topography interaction. Wang (1992) used both a contour dynamics model and a primitive equation model to consider barotropic interactions of an anticyclone with sloping topography. Even with the simplest model (the contour dynamics model), a topographic cyclone formed as the anticyclone interacted with the topography, and the vortex pair was seen to drive cross-topography exchange.

McWilliams and Flierl (1979) used a quasigeostrophic (QG) model with two vertical modes to show that a nonlinear baroclinic vortex can generate a barotropic vortex pair as it evolves. Mied and Lindemann (1979) showed that a two-layer primitive equation β plane model could produce the same type of barotropic vortex pair seen by McWilliams and Flierl (1979). Mied and Lindemann (1982) used a two-layer primitive equation β plane model to demonstrate that a barotropic vortex pair can result from the evolution of an upper layer cyclone overlying a deep anticyclone, when horizontal separation exists between the vortex centers.

Hooker and Brown (1994) used a point vortex model to simulate the evolution of a ring-cyclone pair of unequal strengths. Their simulations showed that, in the absence of boundary effects, the weaker cyclone undergoes regular periods of filamentation (when the cyclone is strained into an elongated, filament shape) and axisymmetrization (when the cyclone relaxes to a more axisymmetric shape) as it rotates about the anticyclone, spending about half of its time in each configuration. When the dipole is located near a boundary, the cyclone undergoes additional filamentation when it moves between the anticyclone and the boundary, spending about three-fourths of its time in filamentation. The latter case, which includes boundary effects representative of the presence of the MAB shelf, agreed well with analysis of the satellite imagery.

Modon solutions represent exact nonlinear solutions that describe the dynamics

of multipole vortices. The development of modon theory in oceanography results from the search for exact solutions to the nonlinear QG equations of motion, with the restriction that the solution's potential vorticity distribution be at least piecewise continuous. Stern (1975) and Larichev and Reznik (1976) provided the first such solutions for a barotropic fluid on a β plane. Their solutions were steadily translating multipole vortices with piecewise continuous potential vorticity. Flierl *et al.* (1980) extended these solutions to a two-layer fluid and demonstrated that the inclusion of baroclinic effects admits much richer solution dynamics.

Steadily rotating modons in a barotropic fluid were first described by Mied *et al.* (1992). These modons did not translate, but could rotate either clockwise or anti-clockwise, existing over either a flat bottom or over an isolated seamount. Kirwan *et al.* (1995) extended the rotating modon solution to include baroclinic effects. Of course, inclusion of baroclinicity produced much richer solution behavior. Recently, Hooker *et al.* (submitted manuscript) used the rotating barotropic modon solution described by Mied *et al.* (1992) to model the kinematic behavior of a WCR dipole system consisting of WCR 82B and an associated peripheral cyclone. A distribution of fluid parcels representing an initial isotherm "fan" was allowed to evolve, and the simulated "streaklines" were compared to satellite surface temperature imagery at various times. The barotropic modon solution was translated kinematically for this study, using observed locations for the dipole center. Good qualitative agreement was achieved between the simulated streakline distributions and the temperature fields shown in the imagery.

1.6 Overview of This Research

It is important to understand how this new model for Gulf Stream rings (as multipole systems) impacts our understanding of mesoscale dynamics, particularly near the shelf break. This study will address the following question concerning ring

systems:

- *What are the implications of multipole ring dynamics at the coastal–open ocean interface?*

Following the suggestion of Kennelly *et al.* (1985) and Churchill *et al.* (1986), a WCR ring system will be modeled as a rotating baroclinic modon, using the solution described by Kirwan *et al.* (1995). Like Hooker *et al.* (submitted manuscript), the simulation will be based on observations of WCR 82B and one peripheral cyclone, since these observations represent the most complete set available for a ring system. This study will improve on the point vortex modeling done by Hooker *et al.* (1994) by including baroclinic effects.

Two characteristics of the rotating baroclinic modon model make it particularly well suited for dynamically modeling the WCR 82B system. First, the model readily admits dipole solutions with vortices of unequal strength, and it describes steady rotation of the cyclone around the anticyclone. As discussed in Hooker and Brown (1994), the cyclone that we are focusing on was observed for a five week period to orbit WCR 82B anticyclonically with an orbit period of about 25 days. The fact that the cyclone maintained a steady rotation rate and was observed for nearly two complete orbits suggests that the dipole rotation was a consequence of the system's dynamics, rather than a transient phenomenon. Second, because the model has two layers, it readily admits baroclinic motions, which are expected to be dynamically important for this system. The desire to admit full baroclinic effects eliminates both point vortex models and contour dynamics models as possible candidates, since, to our knowledge, they have not been applied to the complete two-layer problem. Note that the baroclinic modon model cannot account for the observed ring translation; however, we have purposefully chosen to focus on system rotation rather than translation in order to assess its importance to the system's dynamics.

Rather than simply reproducing the kinematic behavior inferred from satellite surface temperature imagery, as was done in Hooker *et al.* (submitted manuscript), this simulation will focus on detailed comparisons between the model dipole and observations. The model's input parameters will be rigorously constrained using the observations so that direct comparisons are justified. The simulation will be constrained by the following observed quantities (Joyce and Kennelly, 1985; Kennelly *et al.*, 1985; Hooker and Brown, 1994):

- environmental parameters (layer depths, stratification, Coriolis);
- distance between the ring and cyclone centers;
- rate of rotation of the cyclone center around the ring's center;
- peak ring and cyclone vorticity;
- peak ring and cyclone azimuthal velocity;
- radius to peak ring and cyclone azimuthal velocity.

It is important to understand at the outset that this model has a large number of input parameters, and that the number of observations that are useful for constraining the model's parameters are limited. As a result, objective comparisons between the simulation and independent observations to assess this application of the model are limited. One assessment will be to compare the model's estimated ring available potential energy (APE) to an estimate derived from a reduced gravity model. Additionally, several flow features inferred from satellite surface temperature imagery will be simulated with the model by allowing patches of fluid particles to evolve over a period of several days. Comparison of these evolutionary results with the imagery permits limited assessment of the simulation.

Once the applicability of the simulation to the observed system has been demonstrated, the model will be used to calculate several quantities that are not directly

observable (ring kinetic energy, dipole energies, volume transport, lower layer velocities). Also, the model will be used to estimate the location of the ring and cyclone perimeters.

Section 2 contains the research questions to be addressed by this study. Section 3 describes the baroclinic modon solution, and section 4 addresses how the model's input parameters will be constrained using information from observations. Section 5 presents the results of the simulation, and a discussion of the results, and a statement of conclusions, is contained in section 6.

2 Research Questions

The following questions will be addressed:

- How do the ring and cyclone velocity profiles from the modon simulation of the WCR 82B system compare to observations?
- Does the simulated cyclone orbit the ring at the same rate that is estimated for the WCR 82B system from analysis of sequential surface temperature imagery?
- Which aspects of the surface layer flow kinematics for the WCR 82B system, inferred from satellite sea surface temperature imagery, can be accounted for by the kinematics of the model?
- Can the model be used to locate the position of the ring and cyclone perimeters? This boundary should exactly enclose the region of “recirculating” water in each vortex.
- Is the estimated volume transport through a section representative of the MAB shelf-slope front consistent with a transport estimate for a shelf water entrainment by WCR 82B based on hydrography and velocity measurements?
- Are the estimated ring energies from the model consistent with estimates made using a reduced-gravity diagnostic model of WCR 82B?
- How do the estimated energies for the *dipole system* compare with energy estimates for the ring?

- What can the dynamics of the model reveal about the structure of the subsurface flow field associated with a dipole? Is this lower layer flow consistent with limited velocity measurements made in the deep ocean layer below WCR's?

3 Description of the Baroclinic Modon Model

3.1 Introduction

The baroclinic modon model is an exact solution to the nonlinear QG potential vorticity equations for a two-layer fluid over a flat bottom. It is recognized at the outset that QG scaling may not be appropriate for all scales of motion that occur in a ring system, since the scales of some observed flow features may be less than the deformation radius. However, QG dynamics can account for many of the larger scale features, and the mathematical and physical simplicity make it an appealing choice at this early stage. We view our approach as a “first step” toward better understanding of the dynamics of multipole QG vortices, and we feel that it will provide valuable insight for solving the complete dynamical problem.

This simulation also represents a preliminary step in modeling the dynamics of multipole ring groups. Kennelly *et al.* (1985) often observed more than one cyclone around WCR 82B. This study, however, focuses on the pairing of a single cyclone with the ring. Larger vortex populations can be easily represented by this model; however, we feel it is prudent to gain some experience and understanding of the simplest multipole case – the dipole.

3.2 The Rotating Baroclinic Modon Model

The setting for the problem considered here is shown in Figure 2. The figure shows a two-layer fluid over a flat bottom with a circular coordinate system. Although the WCR 82B system was observed to move along the MAB slope, the sloping bottom appeared to act more as a steering mechanism for the translating ring system rather than an important vorticity source/sink. This will be discussed in more detail in

section 6.1. The focus here will be on modon solutions, so it will be necessary to develop solutions in three geographic regions. The inner two regions comprise the modons with radii that may be different in each layer, while region III is exterior to both modons.

We expect solutions to be well behaved at the origin, decay to zero at infinite radial distances, and be smooth at region boundaries up to first order derivatives in the streamfunctions. As the model is inviscid, these conditions are not sufficient to ensure continuity of vorticity. In fact, we have found that it is not possible to ensure that vorticity (more accurately potential vorticity) is continuous at the modon boundaries. The reason for this is that the azimuthal structure required for the modons extends into region III, making it impossible to enforce continuity of vorticity across this boundary.

For these conditions, the dimensional potential vorticity equations for the two layers are

$$\partial \hat{q}_i / \partial \hat{t} + \hat{J}(\hat{\psi}_i, \hat{q}_i) = \hat{S}_i(\hat{r}, \theta), \quad i = 1, 2 \quad (1)$$

where

$$\hat{q}_1 = \hat{\nabla}^2 \hat{\psi}_1 - \hat{F}_1 (\hat{\psi}_1 - \hat{\psi}_2) \quad (2a)$$

$$\hat{q}_2 = \hat{\nabla}^2 \hat{\psi}_2 - \hat{F}_2 (\hat{\psi}_2 - \hat{\psi}_1) \quad (2b)$$

$$\hat{F}_1 = f^2 / g' H_1, \quad \hat{F}_2 = f^2 / g' H_2.$$

The potential vorticity sources are \hat{S}_i ; $\hat{\psi}_i$ is the streamfunction for layer i ; \hat{q}_i is the potential vorticity of layer i ; f is the Coriolis acceleration; g' is reduced gravity; and H_i is the undisturbed thickness of layer i . The $\hat{\nabla}^2$ and \hat{J} are the Laplacian and

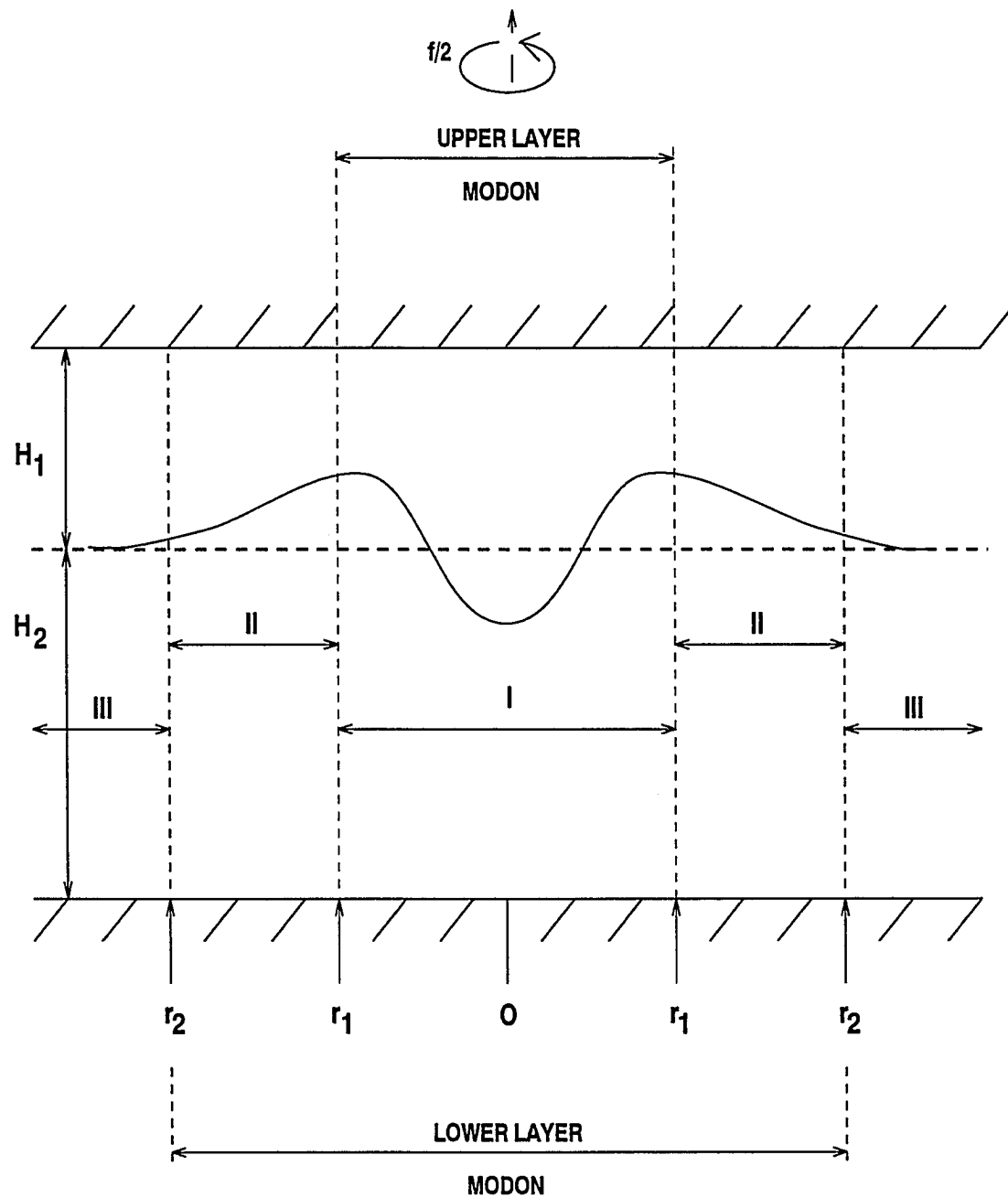


Figure 2: The physical setting for the baroclinic modon model.

Jacobian operators. The coordinate system is circular, with the radial and angular variables denoted by \hat{r} and θ , respectively, and \hat{t} is time. Finally, the $(\hat{})$ indicates dimensional variables, operators or parameters.

As in Kirwan *et al.* (1995), solutions to (1) are sought in the form

$$\hat{q}_i = \hat{q}_i(\hat{r}, \theta - \hat{\omega} \hat{t}), \quad \hat{\psi}_i = \hat{\psi}_i(\hat{r}, \theta - \hat{\omega} \hat{t}).$$

The assumption of steady rotation without change of form reduces (1) to

$$\hat{J}(\hat{\psi}_i - \hat{\omega} \hat{r}^2/2 - \hat{\mathcal{A}}_i, \hat{q}_i) = \hat{S}_i(\hat{r}, \theta - \hat{\omega} \hat{t}). \quad (3)$$

where $\hat{\mathcal{A}}_i$ are constants to be determined later. Given a suitable choice of \hat{S}_i , Eq. (3) states that the \hat{q}_i are general functions of $\hat{\psi}_i - \hat{\omega} \hat{r}^2/2 - \hat{\mathcal{A}}_i$.

Solutions are sought which satisfy

$$\hat{q}_i = \hat{\Gamma}_i(\hat{\psi}_i - \hat{\omega} \hat{r}^2/2 - \hat{\mathcal{A}}_i) \sigma(\hat{r}_i - \hat{r}) \quad (4)$$

where

$$\hat{\Gamma}_i = \hat{\chi}_i - \hat{\kappa}_i^2(\hat{\psi}_i - \hat{\omega} \hat{r}^2/2 - \hat{\mathcal{A}}_i)$$

Here, the $\hat{\Gamma}_i$ are specified linear functions, σ is a generalized (Heaviside) function, and the $\hat{\chi}_i$ and $\hat{\kappa}_i$ are constants.

Substitution of (4) into (3) yields

$$\hat{J}(\hat{\Upsilon}_i, \hat{\Gamma}_i(\hat{\Upsilon}_i)) \sigma(\hat{r}_i - \hat{r}) = 0 \quad (5)$$

everywhere except at $\hat{r} = \hat{r}_i$ and

$$[(\partial \hat{\Upsilon}_i / \partial \theta)(\hat{\Gamma}_i / \hat{r}) \delta(\hat{r}_i - \hat{r})]|_{\hat{r}=\hat{r}_i} = \hat{S}_i(\hat{r}, \theta - \hat{\omega} \hat{t}) \quad (6)$$

where

$$\hat{\Upsilon}_i = \hat{\psi}_i - \hat{\omega} r^2/2 - \hat{Q}_i \quad (7)$$

$$\hat{Q}_i = \hat{\mathcal{A}}_i + \hat{\chi}_i/\hat{\kappa}_i^2$$

and

$$\partial\sigma(\hat{r}_i - \hat{r})/\partial\hat{r} = \delta(\hat{r}_i - \hat{r}).$$

Equation (4) states that discontinuities in potential vorticity occur at the modon boundaries \hat{r}_i , and (5) shows that the source \hat{S}_i provides a jump in potential vorticity for particles crossing the boundaries. From (7), it is seen that the $\hat{\Upsilon}_i$ are continuous everywhere, since the \hat{Q}_i are constants. Furthermore, (5) implies that the $\hat{\Upsilon}_i$ are globally conserved following the fluid motion.

Considering only linear functions for the $\hat{\Gamma}_i$, we express (5) in matrix form as

$$\begin{aligned} \hat{\nabla}^2 \begin{bmatrix} \hat{\psi}_1 \\ \hat{\psi}_2 \end{bmatrix} - \begin{bmatrix} \hat{F}_1 & -\hat{F}_1 \\ -\hat{F}_2 & \hat{F}_2 \end{bmatrix} \begin{bmatrix} \hat{\psi}_1 \\ \hat{\psi}_2 \end{bmatrix} = \\ - \begin{bmatrix} \hat{\kappa}_1^2 \sigma(\hat{r}_1 - \hat{r}) & 0 \\ 0 & \hat{\kappa}_2^2 \sigma(\hat{r}_2 - \hat{r}) \end{bmatrix} \begin{bmatrix} \hat{\psi}_1 - \hat{\omega} \hat{r}^2/2 - \hat{Q}_1 \\ \hat{\psi}_2 - \hat{\omega} \hat{r}^2/2 - \hat{Q}_2 \end{bmatrix}. \end{aligned} \quad (8)$$

In addition to (8) it is necessary to specify conditions to ensure that the solution is well behaved at $\hat{r} = 0, \infty$:

$$\lim_{\hat{r} \rightarrow \infty} \hat{\psi}_i = 0 \quad (9a)$$

$$\lim_{\hat{r} \rightarrow 0} |\hat{\psi}_i| < \infty. \quad (9b)$$

The solutions and their first derivatives in each layer must also be continuous at each modon boundary \hat{r}_i , resulting in smoothness or patch conditions at $y = \hat{r}_i$, which are

$$\lim_{\hat{r} \rightarrow y^-} (\hat{\psi}_i, \partial \hat{\psi}_i / \partial \hat{r}, \partial \hat{\psi}_i / \partial \theta) = \lim_{\hat{r} \rightarrow y^+} (\hat{\psi}_i, \partial \hat{\psi}_i / \partial r, \partial \hat{\psi}_i / \partial \theta). \quad (10)$$

These guarantee that the streamfunction, azimuthal velocity and radial velocity are continuous at the modon boundaries. In all, (9) constitutes 4 conditions while (10) represents 12 separate equations: 3 conditions at 2 boundaries for each of 2 layers.

It is convenient to nondimensionalize (8) by:

$$\hat{\psi}_i = f \hat{r}_m^2 \psi_i$$

$$\hat{r} = \hat{r}_m r$$

$$\hat{\nabla}^2 = (1/\hat{r}_m)^2 \nabla^2$$

$$\hat{\omega} = \omega f$$

$$1/\epsilon = (\hat{r}_m/\hat{r}_d)^2$$

$$(1/\hat{r}_d)^2 = f^2(H_1 + H_2)/g'H_1H_2 = \hat{F}_1 + \hat{F}_2$$

$$\hat{\kappa}_i^2 = \beta_i^{-1}/\hat{r}_m^2$$

$$\hat{Q}_i = f \hat{r}_m^2 Q_i$$

$$\hat{F}_i = F_i/\hat{r}_m^2$$

where \hat{r}_m is the larger of the two modon radii \hat{r}_i , and \hat{r}_d is the internal deformation radius, defined as

$$\hat{r}_d = \sqrt{g'H_1H_2/f^2(H_1 + H_2)} \quad (11)$$

The nondimensional version of (8) is now

$$(\nabla^2 \delta_{ij} + F_{ij}) \psi_j = P_i \quad (12)$$

where δ_{ij} is the unit matrix,

$$F_{ij} = \begin{bmatrix} \beta_1^{-1}\sigma(r_1 - r) - F_1 & F_1 \\ F_2 & \beta_2^{-1}\sigma(r_2 - r) - F_2 \end{bmatrix} \quad (13)$$

and

$$P_i = [(\omega r^2/2 + Q_i)/\beta_i]\sigma(r_i - r) \quad (14)$$

The two coupled equations of (12) can be solved by the method of normal modes. The diagonalizing transformation

$$\mu_{pi} F_{ij} \mu_{jq}^{-1} = \lambda_{\pm} \delta_{pq}$$

reduces (12) to

$$(\nabla^2 + \lambda_{\pm}^{\alpha})\psi_{\pm}^{\alpha} = P_{\pm}^{\alpha}. \quad (15)$$

Here the superscript α refers to the appropriate region in Figure 2.

Kirwan *et al.* (1995) give details for obtaining the elements of μ and the eigenvectors λ_{\pm} , as well as P_{\pm} . They show that the ψ_{\pm} reduce to the classic barotropic and baroclinic modes outside the modons, in region III, or whenever $\beta_1^{-1} = \beta_2^{-1}$. Hence the + and - modes are interpreted here as the modon barotropic and baroclinic modes, respectively.

The individual equations for each region in (15) become

$$(\nabla^2 + \lambda_{\pm}^I)\psi_{\pm}^I = P_{\pm}^I \quad (16)$$

$$(\nabla^2 \pm \lambda_{\pm}^{II})\psi_{\pm}^{II} = P_{\pm}^{II} \quad (17)$$

$$\nabla^2 \psi_+^{III} = 0$$

$$(\nabla^2 - 1/\epsilon) \psi_-^{III} = 0 \quad (18)$$

The solutions to (16–18) are critically dependent upon the sign of λ_{\pm} . Details are discussed in Kirwan *et al.* (1994), and they note that the sign of λ_- is undetermined in region I. For parameter ranges considered here, $\lambda_-^I > 0$. In regions II and III, the negative character of λ_- produces modified Bessel function solutions. This is explicit in (18) and implied in (17) where λ_-^{II} denotes the magnitude of that eigenvalue.

3.3 Solutions

Solutions to (16–18) are straightforward. They are obtained by separation of variables and are composed of radially dependent axisymmetric and azimuthal components. The two (\pm) modes in each of the three regions I, II, and III) are expressed as

$$\begin{aligned} \psi_+^I = & [Q_1/\beta_1 + \mu_+^I Q_2/\beta_2]/\lambda_+^I - 2\omega(1/\beta_1 + \mu_+^I/\beta_2)/(\lambda_+^I)^2 \\ & + r^2[(\omega/2)(1/\beta_1 + \mu_+^I/\beta_2)/\lambda_+^I \\ & + b_{+o}^I J_o[(\lambda_+^I)^{1/2}r] + b_{+n}^I J_n[(\lambda_+^I)^{1/2}r] \sin n\theta \end{aligned} \quad (19)$$

$$\begin{aligned} \psi_-^I = & [Q_1/\beta_1 + \mu_-^I Q_2/\beta_2]/\lambda_-^I - 2\omega(1/\beta_1 + \mu_-^I/\beta_2)/(\lambda_-^I)^2 \\ & + r^2[(\omega/2)(1/\beta_1 + \mu_-^I/\beta_2)/\lambda_-^I \\ & + b_{-o}^I B_o[(\lambda_-^I)^{1/2}r] + b_{-n}^I B_n[(\lambda_-^I)^{1/2}r] \sin n\theta \end{aligned} \quad (20)$$

$$\begin{aligned}
\psi_+^{II} = & [(Q_1/\beta_1)\sigma(r_1 - r) + (\mu_+^{II}Q_2/\beta_2)\sigma(r_2 - r)]/\lambda_+^{II} \\
& - 2\omega[(1/\beta_1)\sigma(r_1 - r) + (\mu_+^{II}/\beta_2)\sigma(r_2 - r)]/(\lambda_+^{II})^2 \\
& + r^2[(\omega/2\beta_1)\sigma(r_1 - r) + (\mu_+^{II}\omega/2\beta_2)\sigma(r_2 - r)]/\lambda_+^{II} \\
& + b_{+o}^{II}J_o[(\lambda_+^{II})^{1/2}r] + c_{+o}^{II}Y_o[(\lambda_+^{II})^{1/2}r] \\
& + \{b_{+n}^{II}J_n[(\lambda_+^{II})^{1/2}r] + c_{+n}^{II}Y_n[(\lambda_+^{II})^{1/2}r]\} \sin n\theta
\end{aligned} \tag{21}$$

$$\begin{aligned}
\psi_-^{II} = & -[(Q_1/\beta_1)\sigma(r_1 - r) + (\mu_-^{II}Q_2/\beta_2)\sigma(r_2 - r)]/\lambda_-^{II} \\
& - 2\omega[(1/\beta_1)\sigma(r_1 - r) + (\mu_-^{II}/\beta_2)\sigma(r_2 - r)]/(\lambda_-^{II})^2 \\
& - r^2[(\omega/2\beta_1)\sigma(r_1 - r) + (\mu_-^{II}\omega/2\beta_2)\sigma(r_2 - r)]/\lambda_-^{II} \\
& + b_{-o}^{II}I_o[(\lambda_-^{II})^{1/2}r] + c_{-o}^{II}K_o[(\lambda_-^{II})^{1/2}r] \\
& + \{b_{-n}^{II}I_n[(\lambda_-^{II})^{1/2}r] + c_{-n}^{II}K_n[(\lambda_-^{II})^{1/2}r]\} \sin n\theta
\end{aligned} \tag{22}$$

$$\psi_+^{III} = c_{+n}^{III}r^{-n} \sin n\theta \tag{23}$$

$$\psi_-^{III} = c_{-o}^{III}K_o(r/\epsilon^{1/2}) + c_{-n}^{III}K_n(r/\epsilon^{1/2}) \sin n\theta. \tag{24}$$

In (19) and (21-24), J_n and Y_n are Bessel function of the first kind, while I_n and K_n are modified Bessel functions. In (19-24), the $b_{\pm n}$ and $c_{\pm n}$ are coefficients associated with the azimuthal solution parts, and the $b_{\pm o}$ and $c_{\pm o}$ are axisymmetric coefficients.

As discussed in Kirwan *et al.* (1995), the sign of λ_-^I is unknown, hence B in (20) is the J Bessel function of the first kind if $\lambda_-^I > 0$, a quartic in r if $\lambda_-^I = 0$, and the I modified Bessel function if $\lambda_-^I < 0$. In general, solutions to (16-18) involve sums over an infinite number of azimuthal modes. However, as discussed in Mied *et al.* (1992),

the underlying nonlinear partial differential equations admit only one such mode as a solution. This is because the patch conditions (10) establish a unique functional relationship among the λ_{\pm} for a single $(\sin n\theta)$ mode. The absence of Y_n and K_n functions in region I and r^n and I_n functions in region III is a consequence of the asymptotic conditions (9a, b).

The solutions to the modal equations, (16–18), are given by (19–24). However, the smoothness conditions apply to the layers, not the modes. The transformation from modes (\pm) to layers ($i = 1, 2$) is described in detail in Kirwan *et al.* (1995) and is given by

$$\psi_1 = (\mu_- \psi_+ - \mu_+ \psi_-)/(\mu_- - \mu_+) = (\delta_- \psi_+ - \delta_+ \psi_-)$$

$$\psi_2 = (\psi_- - \psi_+)/(\mu_- - \mu_+) = \delta(\psi_- - \psi_+).$$

This transformation must be applied to each region and the patch conditions (10) applied to each of the boundaries in each layer. The result of these continuity requirements is a linear algebraic system of 12 equations; however, some simplification of this system is readily achieved.

The restriction of the solution to a single azimuthal mode (of arbitrary order) means that the four $\partial/\partial\theta$ patch conditions are trivially satisfied by aligning the phases in the solutions in each of the regions. The result of this simplification is an algebraic system of eight equations. This was anticipated from Mied *et al.* (1992) and incorporated in (19–24).

Application of the patch conditions results in eight homogeneous equations for the eight azimuthal coefficients. The necessary condition that this system possess a nontrivial solution for the coefficients is that the determinant of the associated eight by eight matrix vanish. This condition indicates that the β_i^{-1} are not independent. This is discussed in detail in Kirwan *et al.* (1995), where the β_i^{-1} are interpreted as modon wave numbers. Since their inverses indicate the length scale of the modon in

that layer, an increase (decrease) in either β_i^{-1} means that the length scale in that layer must decrease (increase).

Rather than simply choosing one β_i^{-1} arbitrarily and fixing the remaining β_i^{-1} to zero the eight by eight determinant, we have elected to constrain the inverse β_i^{-1} to approximate integer radial mode numbers in each layer. As a result, two layer radial mode numbers p_i are chosen, and β_i^{-1} values corresponding to the approximate p_i are found numerically. As discussed in Kirwan *et al.* (1995), determinant values describe a saddle point at the intersection of exact integer (p_1, p_2) pairs, so a simple numerical scheme is used to find a (β_1, β_2) pair that precisely zeroes the eight by eight determinant as closely as possible to the saddle point.

Further numerical analysis of the determinant showed that it was of order seven. This means that of the eight azimuthal coefficients one may be chosen arbitrarily, with the values of the other seven linearly dependent upon the chosen coefficient. We have elected to express all of the $b_{\pm n}$ and $c_{\pm n}$ in (19–24) in terms of b_{+n}^I .

The patch conditions (10) applied to (19–24) also yield eight equations for the axisymmetric quantities, just as for the azimuthal terms. Moreover, one axisymmetric streamfunction amplitude in each layer (Ψ_1 and Ψ_2) must be prescribed at $\hat{r} = 0$. That is,

$$\psi_1(0) = \Psi_1$$

$$\psi_2(0) = \Psi_2.$$

These two rider conditions, along with the eight patch conditions, result in a system of 10 linear equations which must be solved numerically. Their solution then yields the values of the 10 remaining modon parameters ($Q_1, Q_2, \omega, b_{\pm o}^I, b_{\pm o}^{II}, c_{\pm o}^{II},$ and c_{-o}^{III}) in terms of Ψ_1 and Ψ_2 .

The model's adjustable parameters are summarized in Table 1. Section 4 will address the sensitivity of the model to variations of the most important of these

parameters and discuss the method used to constrain the model's parameters using observations of the WCR 82B system.

Table 1: Summary of baroclinic modon model parameters

Environmental parameters	
Upper layer mean thickness	H_1
Lower layer mean thickness	H_2
Reduced gravity	g'
Coriolis acceleration	f
Geometric parameters	
Azimuthal mode number	n
Upper layer radial mode number	p_1
Lower layer radial mode number	p_2
Upper layer modon radius	\hat{r}_1
Lower layer modon radius	\hat{r}_2
Arbitrary amplitudes	
Region I barotropic mode amplitude	b_{+n}^I
Upper layer axisymmetric rider	Ψ_1
Lower layer axisymmetric rider	Ψ_2

4 Sensitivity of the Model to Parameter Changes

4.1 Background

Before the baroclinic modon model is used to simulate the dynamics of a physical system, it is appropriate to consider how the model responds to variations in the adjustable parameters shown in Table 1. A detailed sensitivity analysis would require systematic variation of each of the 12 parameters shown in Table 1. Clearly, this is not feasible. Alternatively, solution derivatives, with respect to each parameter, could be evaluated in the neighborhood of a specific parameter choice. This method was not attempted. Rather, since this work focuses on the dynamics of a single dipole, physical insight available from the observations of the WCR 82B vortex pair, coupled with some elementary understanding of the model's behavior, will be used to reduce the sensitivity analysis to the three most dynamically important parameters.

To achieve this reduction, two estimates of internal deformation radius \hat{r}_d will be used to fix the environmental parameters H_1 and H_2 , using values of g' and f_0 appropriate for the WCR 82B system. Then we will simply fix the mode numbers (n, p_1, p_2) at values that correspond to the simplest dipole solution. Also, an estimate of the distance between the centers of the ring and cyclone will be used to fix the upper layer modon radius \hat{r}_1 . Finally, an estimate of the orbit rate ω of the cyclone around the ring's center, obtained from analysis of sequential satellite images, will be used to fix Ψ_2 for a specified Ψ_1 .

The next three sections provide a detailed description of how values for the nine fixed parameters were chosen. The sensitivity analysis will consist of varying the remaining three parameters, \hat{r}_2 , Ψ_1 , and b_{+n}^I to determine their effects on the model's

behavior.

4.2 Choosing the Environmental Parameters

Two of the model's four environmental parameters will be fixed for the sensitivity analysis. The Coriolis acceleration, f_0 , is chosen as $9.175 \times 10^{-5} \text{ rad s}^{-1}$ based on a representative latitude of 39° . Reduced gravity, g' , is chosen as 0.0106 m s^{-2} . This value is an empirical estimate, based on a regression fit of dynamic height to the depth of the 10° isotherm for a CTD section through WCR 82B described by Olson *et al.* (1985).

Two cases will be examined for the remaining two environmental parameters, H_1 and H_2 . Layer thicknesses corresponding to two different values for internal deformation radius \hat{r}_d are chosen, while the total water column depth, $H = H_1 + H_2$, remains fixed.

This study will focus on the dynamics of the rotating dipolar structure detailed by Hooker and Brown (1994) for the period 29 March 1982 (day 88) through 4 May 1982 (day 124). The track of WCR 82B's center for this period is shown between points C and D in Figure 1 of Evans *et al.* (1985). A representative water depth along this portion of the track is 2700 m, the value chosen for the model's total depth H .

The internal deformation radius, \hat{r}_d , is defined in (11). The sensitivity analysis will compare model results for two values of \hat{r}_d . The first value, 26.4 km, is the \hat{r}_d estimate for WCR 82B during April 1982 made by Olson *et al.* using a diagnostic two-layer model. The second value, 19.2 km, is the mean annual value reported by Emery *et al.* (1984) for the 5° box that includes the observed path of WCR 82B.

Equation (11) was used to compute values for H_1 and H_2 based on the above choices for f , g' , H , and \hat{r}_d . The resulting H_1 and H_2 are 777 m and 1923 m for $\hat{r}_d = 26.4 \text{ km}$, and 334 m and 2366 m for $\hat{r}_d = 19.2 \text{ km}$.

4.3 The Geometric Parameters

A total of five geometric parameters must be specified for the model. Four of these will be fixed for the sensitivity analysis: n , p_1 , p_2 , and \hat{r}_1 . The remaining parameter, \hat{r}_2 , will be varied to determine its effects on the model's behavior.

Because the ring-cyclone pair is taken to be a dipole, all three of the mode numbers have been fixed at a value of one. These mode numbers result in a single maximum and minimum for the solution, establishing the basic dipolar structure. Kirwan *et al.* (1995) contains a study of the effects of changing mode numbers on the baroclinic modon solution. They note that the azimuthal mode number n determines the number of vortices of each sign that occur in the azimuth, with $n = 1$ corresponding to the dipole case. They also note that the radial mode numbers p_i determine the number of vortices present along a radial line directed outward from the origin in each layer. Examples of solutions for various mode number combinations over a flat bottom are shown in Figure 7 of Kirwan *et al.* (1995).

The upper layer modon radius \hat{r}_1 defines a natural length scale for the model solution in the upper layer. The distance between the centers of the ring and cyclone is sensitive to \hat{r}_1 variations, while changes in other parameters affect this distance only modestly. Based on an observed distance of 70–90 km between the center of the ring and an associated cyclone, reported by Kennelly *et al.* (1985), a value of $\hat{r}_1 = 75$ km was chosen. This \hat{r}_1 value results in a center to center distance of 70 km for the dipole in the model's upper layer.

4.4 The Lower Layer Rider Amplitude

As discussed in section 3, the orbit rate ω of the cyclone around the ring's center is a linear function of the upper and lower layer rider amplitudes, Ψ_1 and Ψ_2 . Since little is known about the structure of the lower layer for the WCR 82B system, the estimated ω of $14.5^\circ \text{ d}^{-1}$ reported by Hooker and Brown (1994) for WCR 82B and

one associated cyclone will be used to determine Ψ_2 for the sensitivity analysis. Once Ψ_1 is chosen, the Ψ_2 value corresponding to the desired ω is determined numerically.

4.5 Evaluating the Model's Sensitivity

As indicators of the model's response to variations in the three chosen parameters, two kinematic quantities will be calculated for both the ring and the cyclone: peak azimuthal velocity (V_{ring}, V_{cyc}) and radius to peak azimuthal velocity (R_{ring}, R_{cyc}). These model quantities will be compared with observations of the WCR 82B system to evaluate the model's sensitivity to parameter changes. Note that V_{ring} will be negative since the ring's circulation is anticyclonic.

For a vortex dipole, radial velocity profiles relative to either the ring or cyclone center will *not* be axisymmetric. Velocities will be highest in the region between the ring and the cyclone, along the line of centers, where the ring and cyclone circulations are additive. Other radial sections, such as one perpendicular to the line of centers, through the center of the ring (cyclone), will have a lower peak azimuthal velocity, since the contribution from the cyclone (ring) is less along this radius.

The velocity measurements, reported by Joyce and Kennelly (1985) for WCR 82B and by Kennelly *et al.* (1985) for one associated cyclone, were made along several different radial lines relative to the ring or cyclone center. Velocities for WCR 82B were measured along five tracks that describe a star pattern roughly centered on the ring. Cyclone velocity measurements were scattered around the azimuth relative to the estimated cyclone center. Estimates of peak ring or cyclone azimuthal velocity that result from polynomial fits through all available data, therefore, represent values that are azimuthally averaged. For the model, peak azimuthal velocity is determined along a radius perpendicular to the line of centers. Since velocities along this radius have a minimum contribution from the opposite "pole" of the dipole, this estimate should be comparable to an azimuthally averaged value.

Table 2: Observations of WCR 82B system used for evaluating sensitivity study

Indicator	Value	Reference
\overline{V}_{ring}	-0.55 m s^{-1}	Olson <i>et al.</i> (1985)
\overline{R}_{ring}	55 km	Olson <i>et al.</i> (1985)
\overline{V}_{cyc}	$0.40\text{--}0.45 \text{ m s}^{-1}$	Kennelly <i>et al.</i> (1985)
\overline{R}_{cyc}	10–25 km	Kennelly <i>et al.</i> (1985)

The following procedure is used to calculate the four model kinematic indicators. First, the ring and cyclone centers are located along the line of centers. This line runs through the origin of the circular coordinate system and is always oriented north-south. However, the cyclone may be located either north or south of the ring, and the dipole orientation is *not* known a priori. Each center is defined as the point where the total velocity magnitude goes to zero, a stagnation point. The stagnation points are determined numerically along the radii extending northward and southward from the origin. The orientation of the dipole is determined by comparing the signs of the relative vorticity calculated at each of the stagnation points once they are located. After the ring and cyclone centers are found, the peak azimuthal velocities V_{ring} and V_{cyc} are found numerically along radii extending eastward from each center. The radius to V_{ring} and V_{cyc} , relative to the appropriate center, defines R_{ring} and R_{cyc} .

Observed values of the four kinematic indicators for the WCR 82B system are summarized in Table 2. The overbar notation indicates that these values are *observed*, rather than calculated from the model. The ring values shown in Table 2 are for the month of April, 1982, the month most representative of the period analyzed by Hooker and Brown (1994). Joyce and Kennelly (1985) report a value of $\overline{R}_{ring} = 50 \text{ km}$ for the period between day 110 and day 111. Although this value is slightly lower than that shown in Table 2, the value in Table 2 will be used to evaluate the sensitivity results.

The cyclone values in Table 2 are based on a velocity survey conducted in June

1982, after the period analyzed by Hooker and Brown (1994). Although the cyclone surveyed was probably *not* the same cyclone studied by Hooker and Brown (1994), the June, 1982 survey represents the most detailed kinematic study available for a peripheral cyclone. These values will therefore be taken as representative of typical cyclone kinematics for this system. A range of values for both \bar{V}_{cyc} and \bar{R}_{cyc} is shown in Table 2 because the decomposed velocities, reported in Figure 4 of Kennelly *et al.* (1985), do not show a well defined peak in the azimuthal velocity profile. In order to evaluate the sensitivity study results, \bar{V}_{cyc} is chosen as 0.40 m s^{-1} and \bar{R}_{cyc} is chosen as 25 km.

The primary goal of this sensitivity study is to determine the best set of parameters to simulate the dynamics of the WCR 82B system. The quality of the simulation can be evaluated by comparing the four model kinematic indicators with the observed values, resulting in four individual error quantities to be minimized. Simultaneous minimization of four error quantities is quite cumbersome, however, and the use of a single error index E , calculated as a simple sum of the individual errors, greatly simplifies the minimization procedure. Here, E is defined as:

$$E = S \left(\left| \frac{V_{ring} - \bar{V}_{ring}}{\bar{V}_{ring}} \right| + \left| \frac{R_{ring} - \bar{R}_{ring}}{\bar{R}_{ring}} \right| + \left| \frac{V_{cyc} - \bar{V}_{cyc}}{\bar{V}_{cyc}} \right| + \left| \frac{R_{cyc} - \bar{R}_{cyc}}{\bar{R}_{cyc}} \right| \right) \quad (25)$$

where S is an arbitrary scale factor. For this study, S was chosen as 10.

In addition to the four kinematic indicators, model peak vorticities for the ring and cyclone are also calculated. Olson *et al.* (1985) estimates a peak ring vorticity of $-3.9 \times 10^{-5} \text{ rad s}^{-1}$ for April, 1982, using an idealized ring momentum balance. For the cyclone, assuming radially symmetric structure with swirl velocity as a linear function of radius, and $\bar{V}_{cyc} = 0.40 \text{ m s}^{-1}$ and $\bar{R}_{cyc} = 25 \text{ km}$, the estimated peak vorticity is $3.2 \times 10^{-5} \text{ rad s}^{-1}$. Since both of these estimates are derived from idealized momentum balances, they have not been included in the group of kinematic indicators that define

Table 3: Parameter sets used for model sensitivity study

Case	\hat{r}_1 (km)	\hat{r}_2 (km)	\hat{r}_d (km)
1	75	10	26.4
2	75	20	26.4
3	75	30	26.4
4	75	40	26.4
5	75	50	26.4
6	75	90	26.4
7	75	100	26.4
8	75	110	26.4
9	75	120	26.4
10	75	130	26.4
11	75	140	26.4
12	75	150	26.4
13	75	20	19.2
14	75	130	19.2

E. Rather, by taking the ratio of relative vorticity to Coriolis as a measure of the Rossby number, model solutions will be subject to a simple threshold criteria – only solutions with Rossby number less than 1 will be considered.

4.6 Results of Model Sensitivity Study

The sensitivity study consists of 14 different cases. The first 12 cases represent a series of increasing \hat{r}_2 values, with $\hat{r}_d = 26.4$ km. The last two cases examine the effects of reducing \hat{r}_d to 19.2 km, for $\hat{r}_2 = 20$ km and $\hat{r}_2 = 130$ km. A summary of the parameter values used in the sensitivity study is shown in Table 3.

The following procedure was used to determine the minimum error index value E_{min} for each case. With \hat{r}_2 and \hat{r}_d fixed at the values shown in Table 3, a 51x51 square grid of E values, corresponding to ordered pairs of b_{+n}^I and Ψ_1 was calculated. Values of E were then contoured in the (b_{+n}^I, Ψ_1) plane, and the range of b_{+n}^I and/or Ψ_1 values spanned by the grid was adjusted as necessary to bracket a minimum value. The domain was resized, and E values were recalculated using a trial and error method

until a clearly defined minimum was bracketed by the (b_{+n}^I, Ψ_1) domain. Once a minimum was bracketed, the (b_{+n}^I, Ψ_1) pair with the lowest E value was simply selected as representative of the true E_{min} .

Two conditions could occur that would result in an undefined E for a given (b_{+n}^I, Ψ_1) pair. First, the resulting upper layer modon solution may not be dipolar due to a large mismatch in b_{+n}^I (azimuthal) and Ψ_1 (axisymmetric) amplitudes, so that either V_{ring} or V_{cyc} could not be determined, and from (25), E is not defined.

Second, the calculated peak ring or cyclone vorticity for a given (b_{+n}^I, Ψ_1) pair might be greater in magnitude than f_0 . Consistency with the relative vorticity threshold criteria (Rossby number < 1) requires the resulting E to be ignored. Grid points that correspond to undefined E values were ignored in creating contour plots of E .

Figure 3 shows a plot of E_{min} versus \hat{r}_2 for the first 12 parameter sets shown in Table 3. The vertical dotted line at $\hat{r}_2 = 75$ km corresponds to the case where $\hat{r}_2 = \hat{r}_1$. The E_{min} values for the first 12 cases fall into two groups, with each group having its own minimum value. These groups are naturally divided into cases where $\hat{r}_2 < \hat{r}_1$ and where $\hat{r}_2 > \hat{r}_1$. The first group, with $10 \text{ km} \leq \hat{r}_2 \leq 50 \text{ km}$, has a sharply defined E_{min} of 4.95 at $\hat{r}_2 = 20 \text{ km}$. The second group, with $90 \text{ km} \leq \hat{r}_2 \leq 150 \text{ km}$, has a much broader E_{min} profile, with a minimum E_{min} of 3.68 at $\hat{r}_2 = 130 \text{ km}$.

The E_{min} values shown in Figure 3 indicate that two parameter sets, with \hat{r}_2 equal to either 20 km or 130 km, will produce simulations of the WCR 82B system with kinematic characteristics that closely match observations. It is not clear from these results which of these two parameter sets should be chosen. Consequently, some additional information about the resulting model solutions must be evaluated.

The upper panel of Figure 4 shows a plot of the ring's peak relative vorticity magnitude (points marked with squares) and the cyclone's peak relative vorticity magnitude (points marked with triangles) versus \hat{r}_2 for cases 1–12. The plot shows that, for cases where $\hat{r}_2 < \hat{r}_1$, the peak cyclone vorticity tends to be higher than that

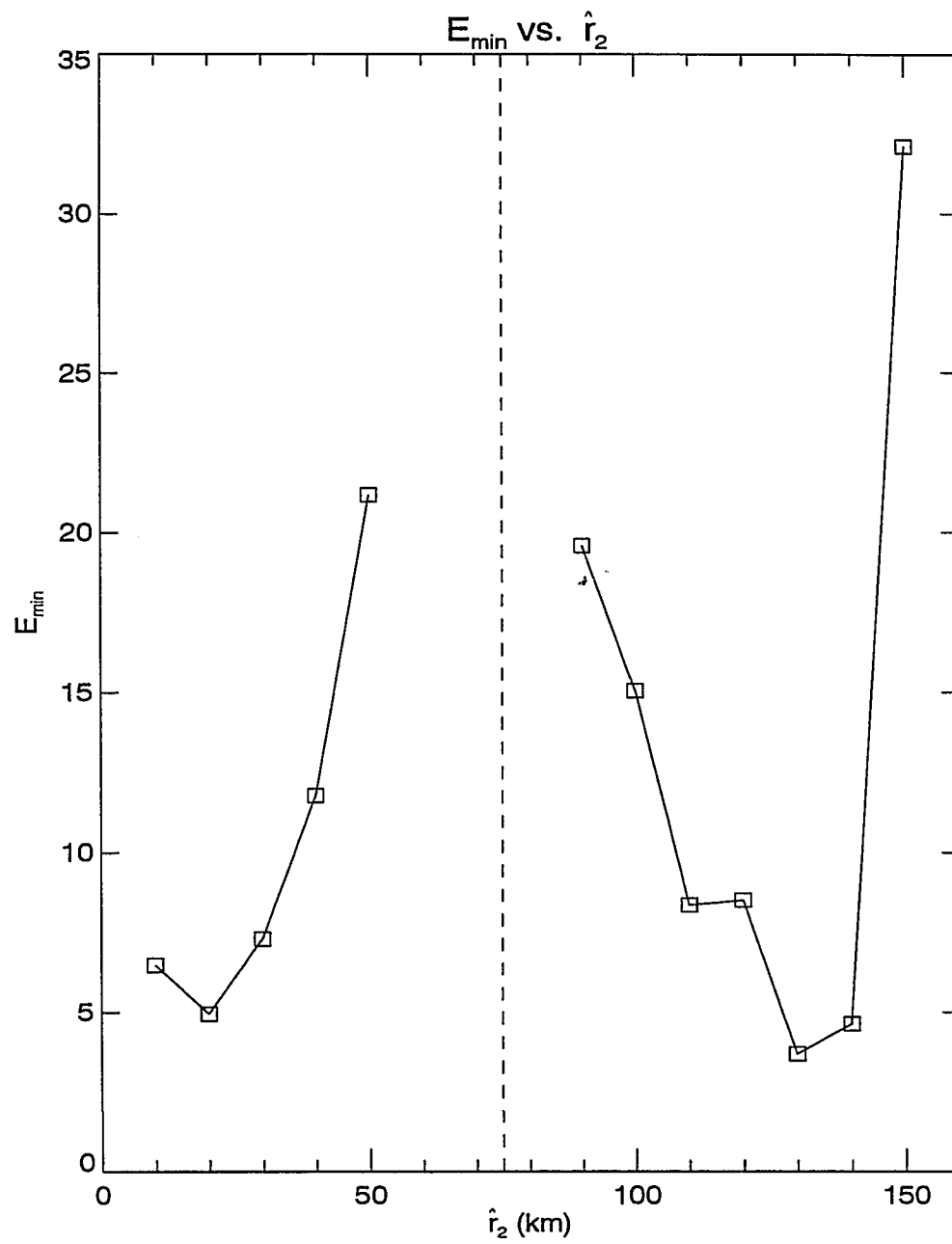


Figure 3: E_{min} versus \hat{r}_2 for the first 12 parameter sets in the sensitivity study.

of the ring. At $\hat{r}_2 = 20$ km, the case with the lowest E_{min} for this group, the peak cyclone vorticity is $8.7 \times 10^{-5} \text{ rad s}^{-1}$, compared to a ring peak vorticity of $3.9 \times 10^{-5} \text{ rad s}^{-1}$. For cases where $\hat{r}_2 > \hat{r}_1$, the peak vorticities tend to be more equal. The case with the lowest E_{min} for this group, with $\hat{r}_2 = 130$ km, has a peak cyclone vorticity of $4.5 \times 10^{-5} \text{ rad s}^{-1}$, compared to a peak ring value of $4.7 \times 10^{-5} \text{ rad s}^{-1}$. Estimates of peak vorticity derived from the observed radial velocity profiles, discussed above, are $3.9 \times 10^{-5} \text{ rad s}^{-1}$ for the ring, and $3.2 \times 10^{-5} \text{ rad s}^{-1}$ for the cyclone, so that the cyclone strength is slightly less than the ring's. A comparison of peak ring and cyclone vorticities, then, suggests that the parameters used for case 10, with $\hat{r}_2 = 130$ km, will better simulate the vorticity behavior of the WCR 82B system, when compared with the parameters used for case 2.

The lower panel of Figure 4 shows a plot of the ring's APE and kinetic energy (KE) versus \hat{r}_2 for cases 1–12. APE values are shown as squares, and KE values are shown as triangles. APE and KE were computed as:

$$APE = \frac{1}{2} \rho_1 g' (h - H_1)^2$$

$$KE = \frac{1}{2} \rho_1 h v^2 \quad (26)$$

following the method of Olson *et al.* (1985) for the upper layer of a two-layer fluid. Here, h is the upper layer thickness and ρ_1 is the upper layer density, chosen as 1025 kg m^{-3} . The boundary of the ring is assumed to be elliptical, with the major axis defined as the radius to maximum azimuthal velocity along a radius extending eastward from the ring's center, and the minor axis defined as the radius to maximum azimuthal velocity along a radius extending northward from the ring's center, away from the cyclone.

The estimated ring APE from Olson *et al.* (1985) for the month of April, 1982

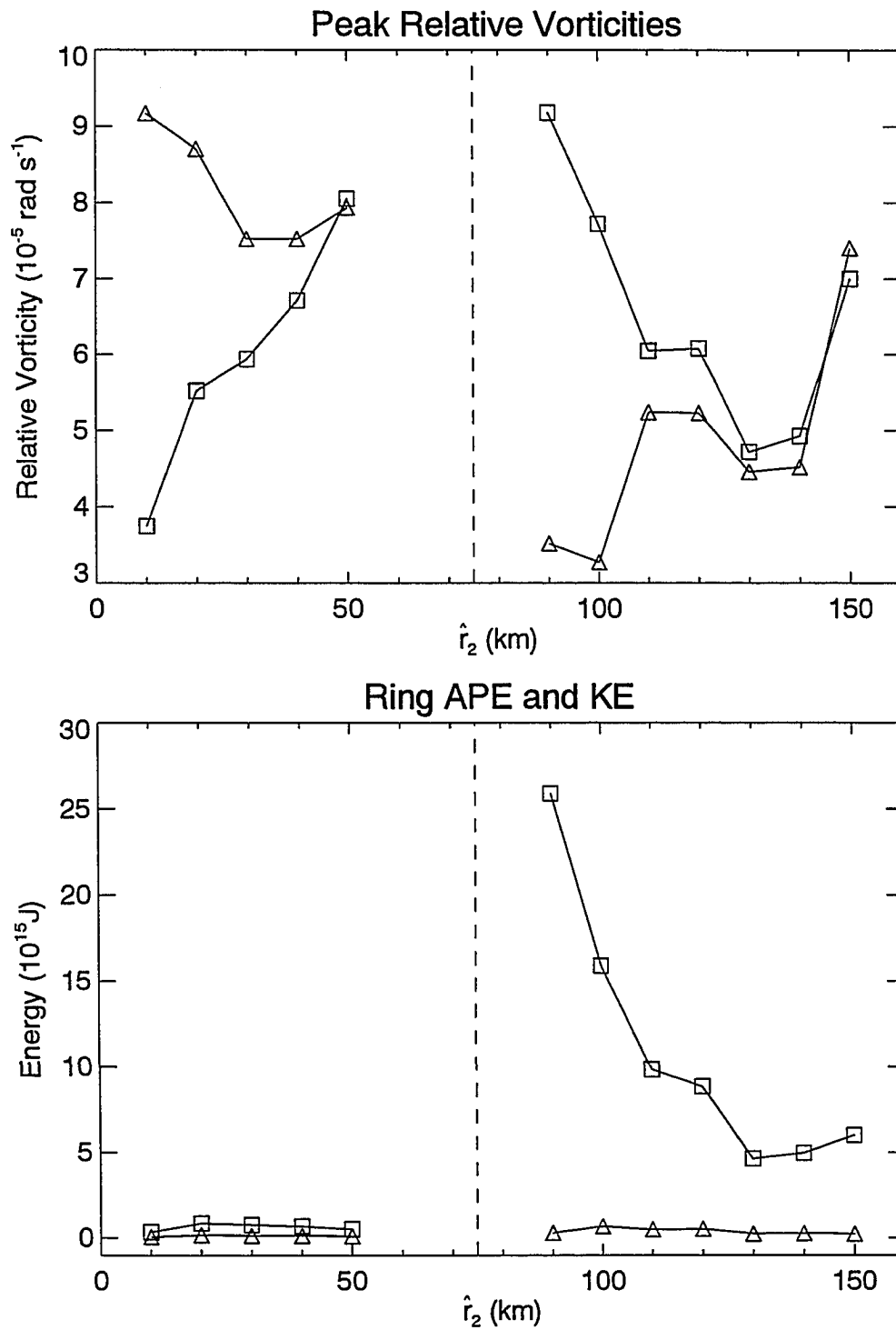


Figure 4: Peak relative vorticities (upper panel) and ring energies (lower panel) versus \hat{r}_2 for the first 12 parameter sets in the sensitivity study.

is approximately 4.1×10^{15} J. The lower panel of Figure 4 shows that, for cases where $\hat{r}_2 < \hat{r}_1$, ring APE values are about 1.0×10^{15} J, roughly one-fourth of the Olson *et al.* (1985) estimate. When $\hat{r}_2 > \hat{r}_1$, ring APE values increase significantly. A consideration of ring APE, then, suggests that cases where $\hat{r}_2 > \hat{r}_1$ will better represent what is known about the ring's energetics.

The Olson *et al.* (1985) estimate of ring APE will be used later as an independent quantity to assess this simulation. Although some knowledge of the ring's energetics was required here to allow a choice to be made between two possible parameter sets, no specific model input parameter was adjusted based on this APE estimate.

The final two cases shown in Table 3 consider the effects of decreasing \hat{r}_d to 19.2 km for the two \hat{r}_2 values that yield the lowest E_{min} values with $\hat{r}_d = 26.4$ km. For case 13, the E_{min} was 7.75, significantly higher than the value of 4.95 for case 2, with $\hat{r}_d = 26.4$ km. For case 14, the E_{min} was 11.54, again significantly higher than the value of 3.68 found for case 10, with $\hat{r}_d = 26.4$ km. These results indicate that reducing \hat{r}_d to 19.2 km degrades the model's ability to reproduce the observed kinematic behavior.

4.7 Summary

The focus of this sensitivity analysis was to determine the best set of model input parameters for simulating the dynamics of the WCR 82B system. By considering a series of \hat{r}_2 values, and looking at solution behavior for each \hat{r}_2 in the (b_{+n}^I, Ψ_1) plane, a single error index E , that measures the deviation of four model kinematic indicators from their observed values, could be minimized. Comparison of E_{min} values for each \hat{r}_2 showed that the 12 cases considered could be split into two groups, each containing its own minimum E_{min} . In addition, the magnitude of E_{min} was comparable in each group (4.95 for case 2 and 3.68 for case 10), making selection of a single parameter set difficult.

When the model's peak ring and cyclone vorticities for cases 2 and 10 are compared

with estimates derived from observed velocity profiles, it is seen that case 10, with $\hat{r}_2 = 130$ km, results in a solution that is more consistent with what we know about the system from observations. When ring energetics are considered, case 10 again is more consistent with observations than case 2, resulting in a ring APE that is comparable to the observed estimate.

Finally, for cases 2 and 10, the effect of reducing \hat{r}_d is examined, resulting in the parameters used for cases 13 and 14. In each case, the reduced \hat{r}_d degrades the model's ability to reproduce the observed kinematic behavior of the WCR 82B system.

This sensitivity study shows that case 10, with $\hat{r}_2 = 130$ km and $\hat{r}_d = 26.4$ km, results in the best match of model characteristics to observations. The parameters for case 10 that correspond to the lowest E value will therefore be used for simulating the dynamics of the WCR 82B system. A summary of all parameter values to be used for this simulation is shown in Table 4. This set of parameters results in a solution that closely matches the radial velocity structure of both the ring and the cyclone with ring and cyclone peak vorticities that are closely matched. In addition, the solution's ring APE exceeds the estimated value derived from observations by only 12%. Results from the simulation will be described in section 4.

Table 4: Parameter values used to simulate the WCR 82B system

Environmental parameters		
Upper layer mean thickness	H_1	777 m
Lower layer mean thickness	H_2	1923 m
Reduced gravity	g'	0.0106 m s^{-2}
Coriolis acceleration	f	$9.175 \times 10^{-5} \text{ rad s}^{-1}$
Geometric parameters		
Azimuthal mode number	n	1
Upper layer radial mode number	p_1	1
Lower layer radial mode number	p_2	1
Upper layer modon radius	\hat{r}_1	75 km
Lower layer modon radius	\hat{r}_2	130 km
Arbitrary amplitudes		
Region I barotropic mode amplitude	b_{+n}^I	1.227×10^{-2}
Upper layer axisymmetric rider	Ψ_1	-8.000×10^{-4}
Lower layer axisymmetric rider	Ψ_2	-3.235×10^{-2}

5 Simulating the WCR 82B System as a Modon

5.1 Introduction

The goal of this simulation is to describe the dynamics of the WCR 82B system, consisting of the ring and one associated peripheral cyclone, for the period 29 March 1982 to 4 May 1982. The parameter values used for this simulation are shown in Table 4.

This simulation consists of two parts. The first part is a diagnostic calculation, which will be used to examine the system's kinematic structure, including velocity profiles for both the ring and cyclone. In addition, three different methods for estimating the location of the ring and cyclone boundaries, based on their velocity structure, will be compared. Finally, the energetics of the system will be examined by calculating APE and KE for the ring, as well as for the entire system.

The second part of the simulation consists of two calculations in which populations of fluid parcels are evolved in time. The first calculation uses three separate patches of fluid to simulate three distinctive flow features apparent in a satellite surface temperature image of the WCR 82B system. The patches are allowed to evolve for a period of 14 days, and their final distribution is compared to satellite imagery. The second calculation examines the evolution of two rectangular fluid patches, each consisting of 2500 regularly spaced fluid parcels, representing MAB shelf water and Gulf Stream water immediately adjacent to the ring-cyclone dipole. These fluid patches are allowed to evolve for several days, and their final distribution is compared to satellite imagery to determine how well the model describes entrainment of surface MAB water and Gulf Stream water readily seen in the imagery.

5.2 Results of the Diagnostic Calculation

5.2.1 Upper Layer Kinematics

The upper panel of Figure 5 shows contours of the upper layer streamfunction ($\hat{\psi}_1$) field with the ring located to the north and the cyclone to the south. All contour plots will follow the same convention: positive contours are shown as solid lines, and negative contours are shown as dashed lines. The contour interval, in $\text{m}^2 \text{s}^{-1}$, is shown in the lower right corner. The dot-dash axes show the location of the origin of the circular coordinate system. Dotted circles, with radii of 75 km and 130 km, show the upper and lower layer modon boundaries, respectively.

The lower panel of Figure 5 shows the velocity vector map for the upper layer. Again, dot-dash axes show the location of the origin, and dotted circles show the location of the upper and lower layer modon boundaries. The centers of the ring and cyclone, defined as zero velocity points, are shown as diamonds. The distance between the ring and cyclone centers is 70 km. A 0.50 m s^{-1} velocity vector, shown at the upper right, provides a measure of velocity scale. The two panels in Figure 5 show that the ring's velocity field is kidney shaped, with lobes extending down around the cyclone. The cyclone's velocity structure is nearly circular.

The $\hat{\psi}_1$ and velocity fields shown in Figure 5 represent the upper layer solution at time zero. It is important to remember that these fields, like all of the fields shown for this simulation, are rotating anticyclonically about the origin with a rotation period of 30.6 inertial periods (24.8 days).

Figure 6 shows a plot of east-west velocity, in m s^{-1} , versus distance from the origin along a north-south section through the line of centers. Positive distances are north of the origin, and negative distances are south. The origin is marked with a dot-dash line, and the location of the ring and cyclone centers are shown as dashed lines. Note that north-south velocity is identically zero along this section, so that east-west velocity has the same magnitude as total velocity. The maximum velocity,

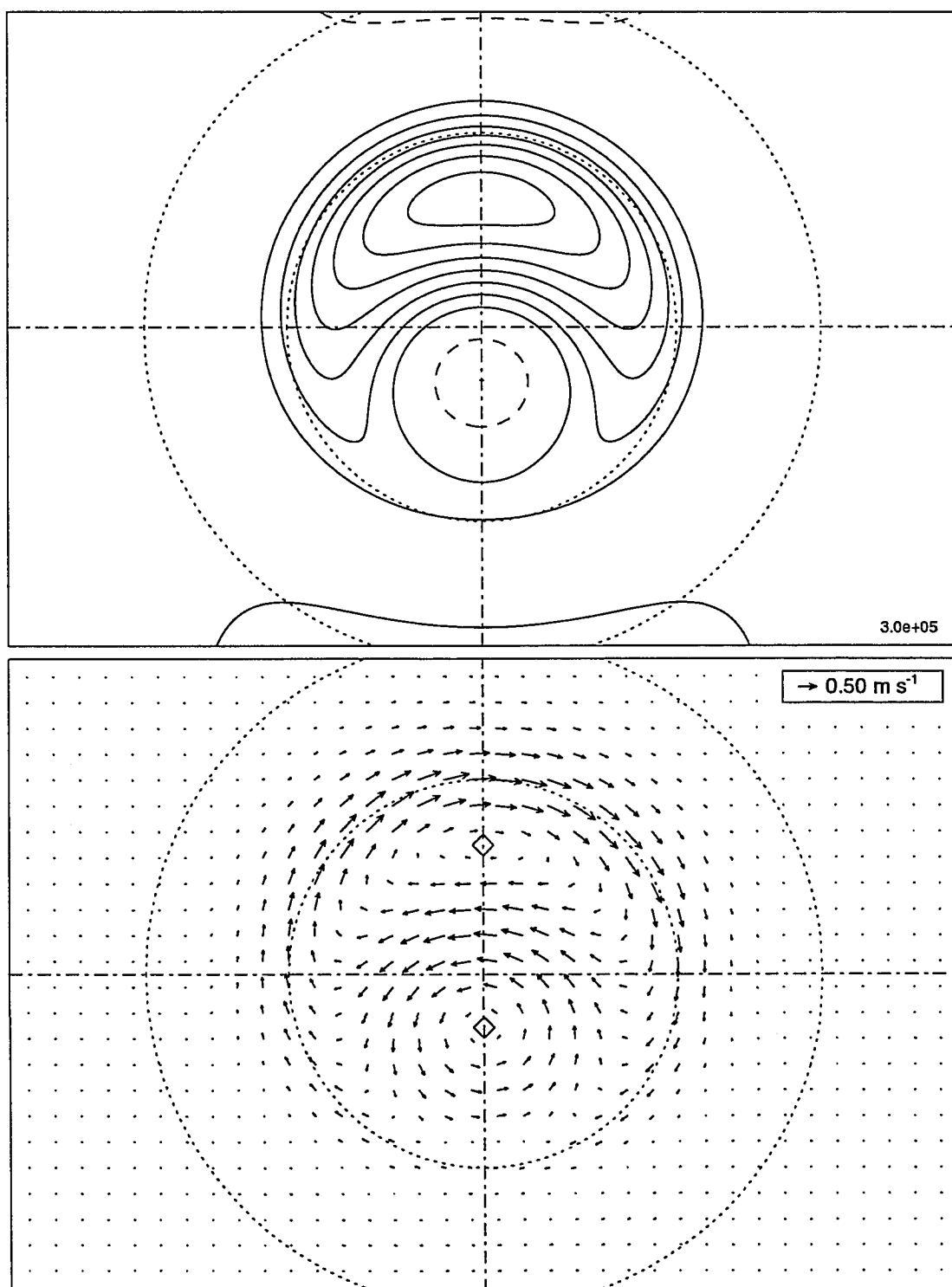


Figure 5: Contours of $\hat{\psi}_1$ field (upper panel) and upper layer velocity vectors (lower panel) for the diagnostic calculation.

0.90 m s⁻¹, occurs at point A, 75 km north of the origin. The minimum velocity, -0.65 m s⁻¹, occurs at point B, 17 km north of the origin. A local maximum velocity of 0.32 m s⁻¹ occurs at point C, 45 km south of the origin. It is interesting to note the the maximum velocity magnitude occurs at the northern edge of the ring and not in the region between the ring and the cyclone. Also, the radius to maximum velocity northward from the ring's center is 25 km, while the radius to maximum velocity southward from the cyclone's center is 24 km. Thus, the ring and cyclone sizes, defined as the radius to maximum velocity, are nearly equal when viewed along this section.

The two upper left panels of Figure 7 show the *observed* velocity profiles for WCR 82B during June, 1982 as reported by Joyce and Kennelly (1985). These velocities were measured with an acoustic Doppler current profiling (ADCP) system. The data points shown are taken from several different radial lines relative to the ring's center, so that the heavy jagged lines represent azimuthally averaged velocity profiles. The smooth curve in the upper left panel shows a polynomial fit of the azimuthal velocity data. Although these observations were made after the time period of the simulation, they will be taken to be representative of the ring during the month of April, 1982 for comparison with the model.

The two panels at the right in Figure 7 show profiles of the model ring's azimuthal and radial velocities along a radial section extending eastward from the ring's center. The velocities are plotted on the same scales as the observed profiles shown at the left, for comparison. The structure of the model's azimuthal velocity profile is similar to the polynomial fit through the observed data in the upper left panel, although the model's peak value of 0.62 m s⁻¹ occurs at 56 km, compared to an observed peak value of 0.55–0.60 m s⁻¹ at 45–50 km (estimated from the polynomial fit curve in the upper left panel). Based on radius to maximum velocity, then, the simulated ring is slightly larger than the observed ring when viewed along a west–east line through the

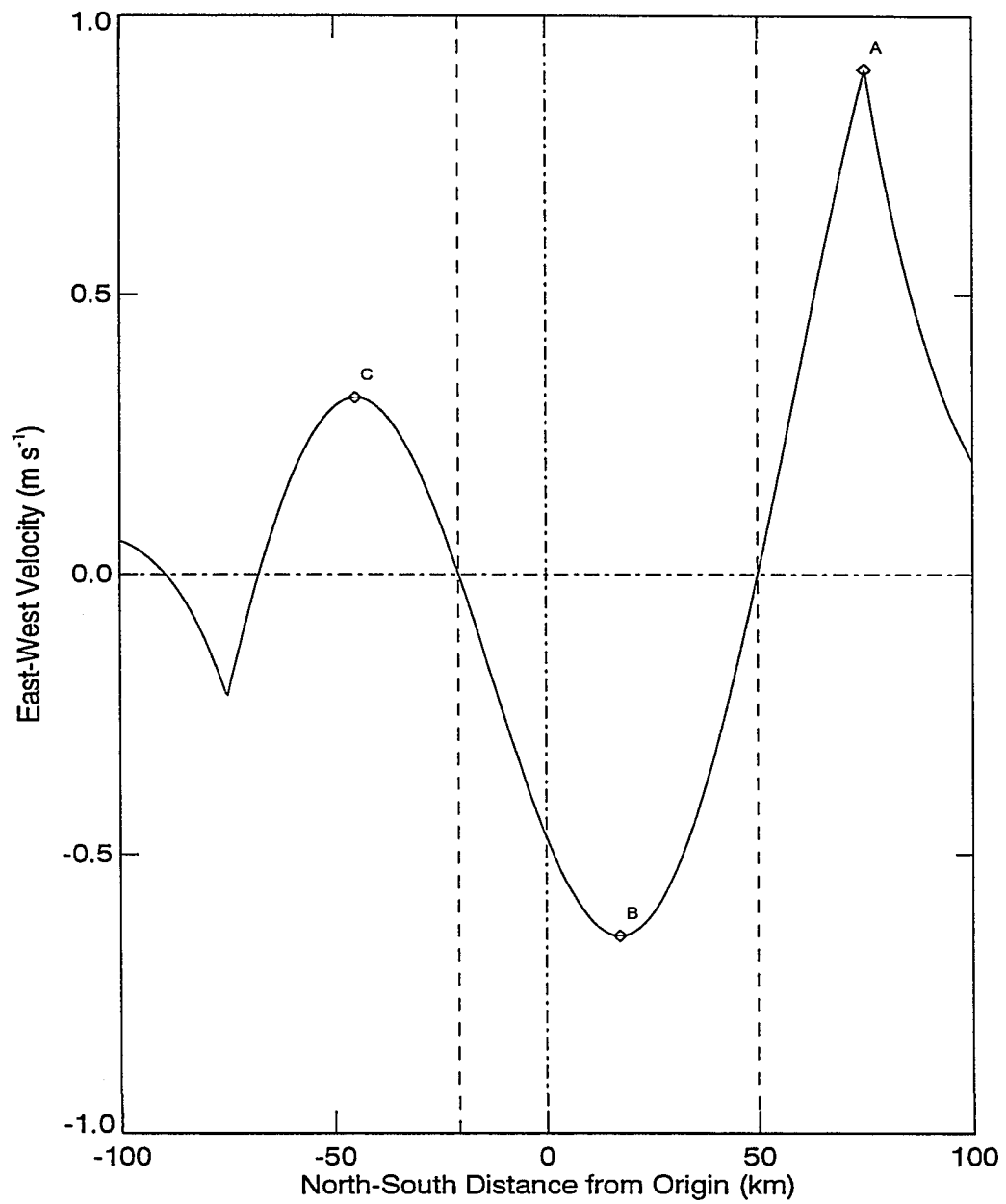


Figure 6: East-west velocity versus distance from the origin along the line between the cyclone and ring centers.

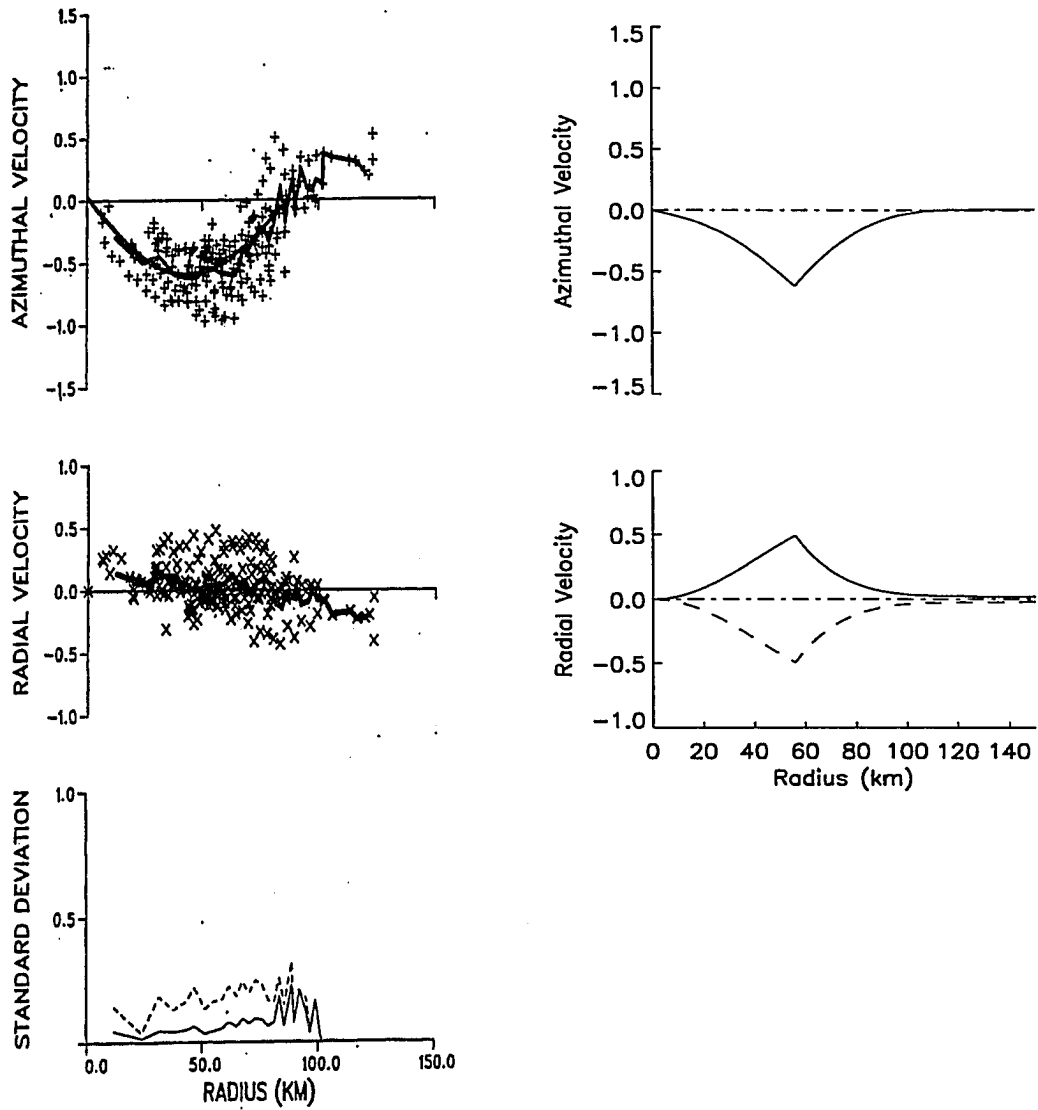


Figure 7: Observed (two upper left panels) and modeled (two right panels) profiles of ring radial and azimuthal velocity. All velocities are in m s^{-1} . Panels at left are taken from Joyce and Kennelly (1985).

ring's center. However, the model ring's maximum azimuthal velocity and radius to maximum azimuthal velocity lie well within the boundaries of the raw data scatter.

Two profiles of radial velocity are shown in the lower right panel of Figure 7. The solid line shows the profile along a radius extending eastward from the ring's center, while the dashed line represents the profile along the radius extending to the west. A peak radial velocity magnitude of 0.49 m s^{-1} occurs at a radius of 56 km along each section. These profiles show that radial velocity is antisymmetric about the ring's center, so that the azimuthally averaged radial velocity would be zero at all radii. This is consistent with the observed average radial velocity profile shown in Figure 7 (left middle panel), which is nearly zero over much of the profile, with peak values no larger than 0.20 m s^{-1} . The structure of the model's radial velocity profile is largely due to the highly elliptical shape of the ring's velocity field, apparent in Figure 5. The model ring's radial velocity profile is quite different from the observed profile. However, uncertainties in locating the precise center of the ring and errors associated with the ADCP measurements (which may be as large as 0.1 m s^{-1}) make estimating the radial component of ring velocity very difficult. The model ring radial velocities, then, are at least consistent with the observations.

The two left panels in Figure 8 show the *observed* ADCP velocity profiles for a peripheral cyclone associated with WCR 82B during June, 1982 as reported by Kennelly *et al.* (1985). The data points shown are taken from several different radial lines relative to the cyclone's center. The solid line in the upper panel represents a fourth-degree polynomial fit of the azimuthal velocity data. As was the case for the ring velocity measurements, these observations were made after the time period of the simulation, but they will be taken to be representative of the peripheral cyclone that was present during the month of April, 1982 to allow for comparison with the model.

The two right panels in Figure 8 show profiles of the model cyclone's azimuthal

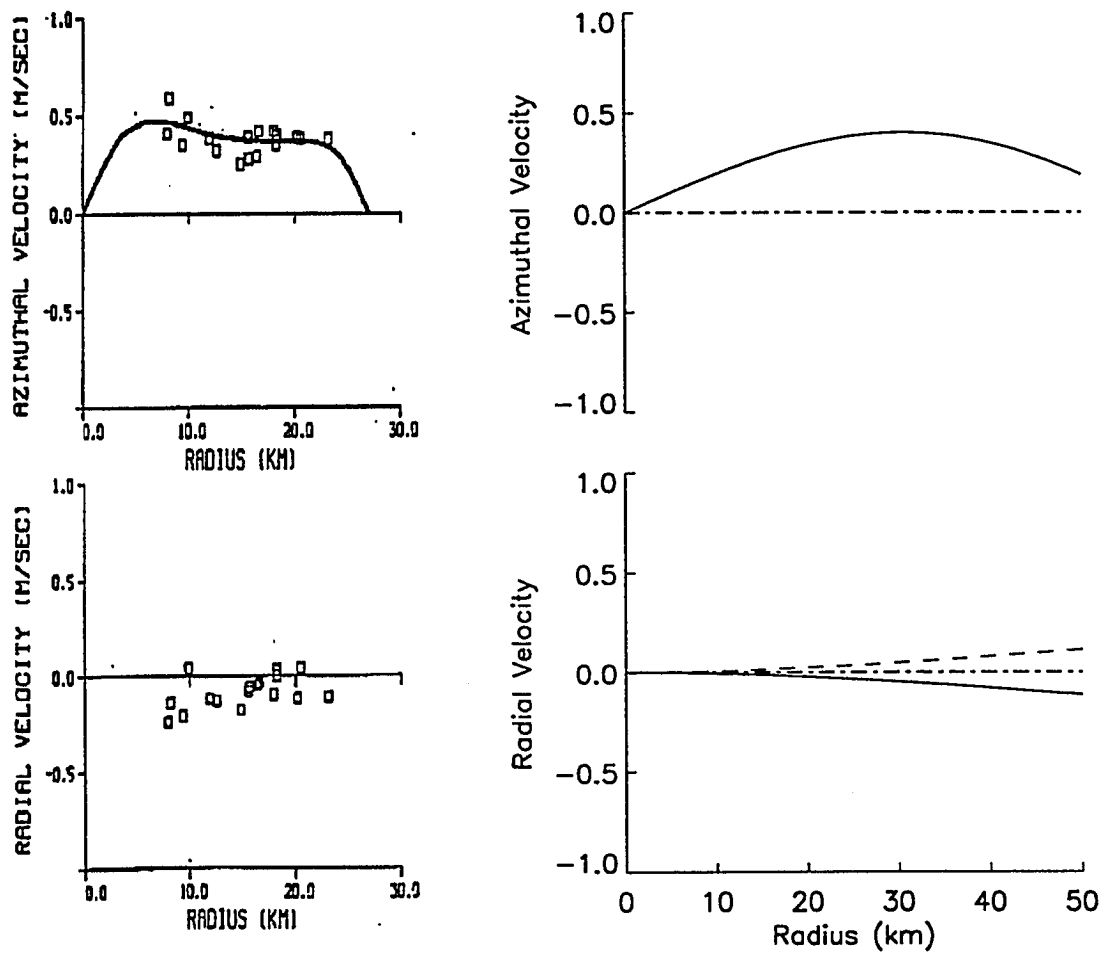


Figure 8: Observed (two left panels) and modeled (two right panels) profiles of cyclone radial and azimuthal velocity. All velocities are in m s^{-1} . Panels at left are taken from Kennelly *et al.* (1985).

and radial velocities along a radial section extending eastward from the cyclone's center. The vertical scales on each plot are the same as those for the observed profiles (left two panels), but the model profiles shown at the right extend to a radius of 50 km so that the model's peak azimuthal velocity can be shown.

The polynomial fit of the observed cyclone azimuthal velocity data (solid line, Figure 8, upper right panel) is quite flat for radii between about 8 km and 25 km with no well-defined peak. The model cyclone's azimuthal velocity profile also has a rather broad appearance, but it does have a peak value (V_{cyc}) of 0.40 m s^{-1} at a radius (R_{cyc}) of 31 km. Remember that the simulation parameters were chosen to minimize errors between these two model values and their observed values ($\bar{V}_{cyc} = 0.40 \text{ m s}^{-1}$ and $\bar{R}_{cyc} = 25 \text{ km}$) as discussed in section 4.

As in the lower right panel of Figure 7, two profiles of radial velocity are shown in the lower right panel of Figure 8, representing sections extending eastward (solid line) and westward (dashed line) from the cyclone's center. A peak radial velocity magnitude of 0.18 m s^{-1} occurs at a radius of 72 km (not shown). As was the case for the ring, the cyclone's radial velocity is antisymmetric about its center, so that an azimuthally averaged model profile would be exactly zero at all radii. Although no attempt was made by Kennelly *et al.* (1985) to apply a polynomial fit to the observed radial velocity data, the model values are of the same order of magnitude as those observed. As with the ring, estimating the observed cyclone radial velocity is quite difficult, so that the model cyclone's radial velocity profile is at least consistent with the observations.

The upper panel in Figure 9 shows contours of the upper layer potential vorticity (\hat{q}_1), as defined in (2a), with the contour interval, in rad s^{-1} , shown in the lower right corner. Here, the mean value of all non-zero points (points inside the modon boundary) has been subtracted from the \hat{q}_1 values for plot clarity. Potential vorticity is piecewise continuous in the model and is identically zero at all points outside the

upper layer modon boundary at 75 km (see (4)). This boundary is shown by the dark, irregular circle that results from the contour routine’s attempt to fit the discontinuous data field. Model fluid parcels conserve \hat{q}_1 in a piecewise sense, so that parcels inside the modon boundary follow \hat{q}_1 contours. In addition, experience with the model has shown that a parcel that exits the modon region, crossing into the exterior region where $\hat{q}_1 = 0$, will reenter the modon region with a \hat{q}_1 value identical to the value it had when it last exited.

The lower panel in Figure 9 shows contours of a quantity that may be termed the “effective streamfunction” for the upper layer (\hat{T}_1), as defined in (7). The contour interval, in $\text{m}^2 \text{s}^{-1}$, is shown in the lower right corner. This quantity is important because it is globally conserved following fluid motion, as discussed in section 3, and plots like the one shown in the lower panel of Figure 9 are useful for predicting fluid parcel behavior in evolutionary calculations. Closed contours of \hat{T}_1 define regions where fluid parcels are “trapped.”

5.2.2 Locating the Ring and Cyclone Perimeters

Estimating the position of the ring or cyclone perimeter is not a straightforward task. Using satellite images of surface temperature, some estimate of the size and shape of a ring can be made by considering a bounding isotherm, particularly for the ring, which often has a clear surface temperature signature. Smaller scale features, like cyclones, however, are often obscured in surface temperature images, making estimates of their geometry difficult. Shape estimates based on surface temperature distributions are closely tied to the features mass field, since surface temperature can be considered as an “alias” for the density field over short time spans.

When hydrographic or velocity information is available for a ring or cyclone, size estimates are normally tied to the feature’s velocity field. The size of a warm-core ring, for example, is often based on the observed radius to maximum velocity. This

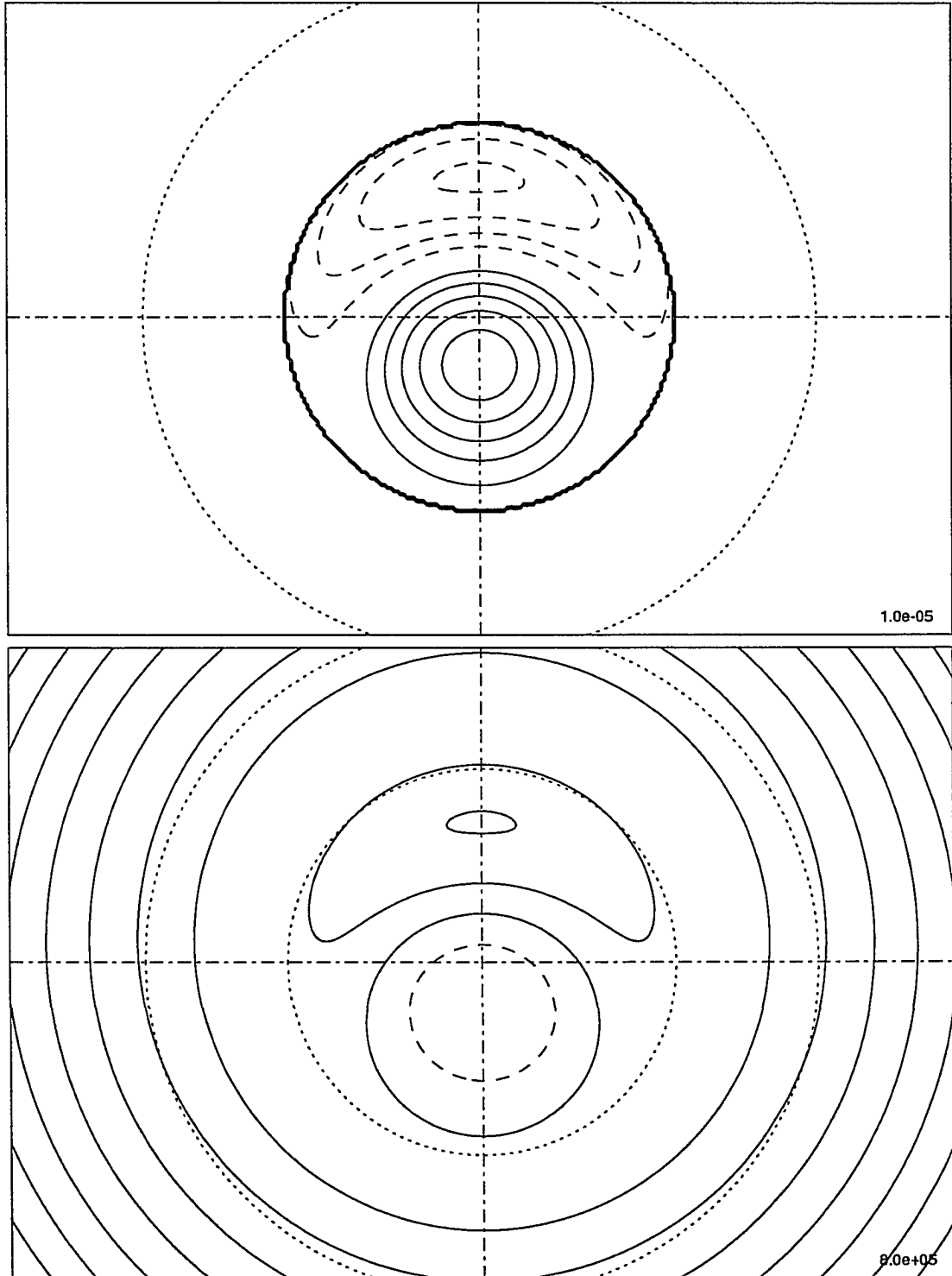


Figure 9: Contours of \hat{q}_1 (upper panel) and \hat{T}_1 (lower panel) for the diagnostic calculation.

is also the case for estimates of the size of peripheral cyclones around WCR 82B discussed by Kennelly *et al.* (1985). Shape estimates based on the velocity field are much more difficult, however, since velocity information is normally gathered asynoptically from many different points around the feature's azimuth, and the data is often azimuthally averaged to yield an *average* radius to maximum velocity. This averaging obscures a feature's elliptical structure, so that the resulting radius estimate provides only a rough measure of the feature's size.

Simulating the WCR 82B system as a modon allows for detailed analysis of the velocity structure of both the ring and cyclone. Model estimates of the ring and cyclone shape will be tied to the model's upper layer velocity field, similar to the method used in analyzing velocity survey information. Data from the model is much more dense than that available from a velocity survey, however, so that no azimuthal averaging will be necessary. The model, then, is uniquely suited to provide insight into the *shape* of these features, in addition to estimates of *size*, based on their velocity structure.

Four different methods were used to estimate the location of the ring and cyclone perimeters. The first three methods define the perimeter location based on the radius to maximum azimuthal velocity (R_{ring}, R_{cyc}), similar to the method used by Joyce and Kennelly (1985) to estimate ring radius, and by Kennelly *et al.* (1985) to estimate the radius of a peripheral cyclone. The last method defines the ring and cyclone perimeters as a curve of constant effective streamfunction \hat{Y}_1 .

The first method attempts to estimate the ring and cyclone perimeters without assuming any specific geometric shape for either feature. One hundred radial sections were equally spaced around the azimuth of each feature, and the radius to maximum azimuthal velocity determined along each section. The result is an estimated feature perimeter consisting of 100 irregularly spaced points. The upper panel of Figure 10 shows the estimated ring and cyclone perimeters, overlaying the upper layer velocity

field, using this method. The centers of the ring and cyclone are shown as diamonds. The unusual shape of the estimated ring perimeter results from two discontinuities in the location of R_{ring} that occur south of the ring center, near the cyclone. The presence of the cyclone complicates the ring's azimuthal velocity structure, and severely limits the usefulness of this method for estimating ring shape. The estimated cyclone perimeter is more regular, but, as before, the presence of the ring skews the perimeter location northward in the region between the ring and cyclone centers.

The second method assumes that the ring and cyclone are ellipses. For the ring, the major ellipse axis is defined as R_{ring} along a section directed eastward from ring's center as shown in the upper right panel of Figure 7. The major axis value is 56 km. The minor ellipse axis is defined as R_{ring} along a section directed northward from the ring's center, away from the cyclone, as shown in Figure 6. The minor axis value is 25 km.

For the cyclone, the major ellipse axis is defined as R_{cyc} along a section directed eastward from cyclone's center, as shown in the upper right panel of Figure 8. The major axis value is 31 km. The minor ellipse axis is defined as R_{cyc} along a section directed southward from the cyclone's center, away from the ring, as shown in Figure 6. The minor axis value is 24 km.

The third method assumes that the ring and cyclone are circles with a radius that results in a circle with the same cross-sectional area as the ellipses constructed in the second method. For the ring, the radius of this circle is 37 km. For the cyclone, the circle's radius is 27 km.

The middle panel of Figure 10 shows both the estimated elliptical perimeters (in blue) and the estimated circular perimeters (in red) overlaying the upper layer velocity field. Again, the ring and cyclone centers are shown as diamonds. Note that, for the ring, both estimated perimeters extend slightly outside the upper layer modon boundary, shown as the inner dotted circle. The ring's velocity structure is

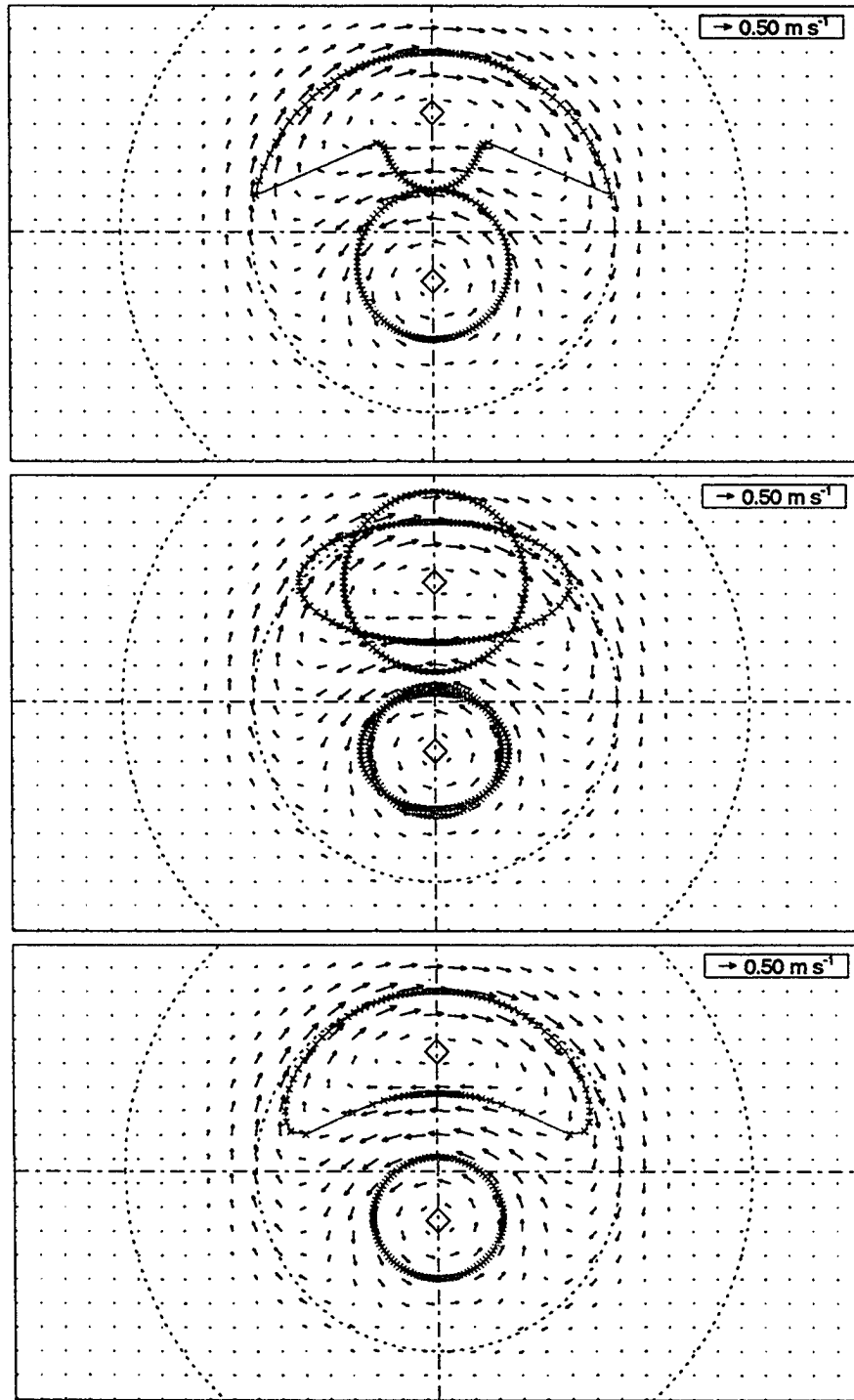


Figure 10: Four methods for estimating ring and cyclone perimeters. Upper panel shows estimate based on location of R_{ring} . Middle panel shows estimate from assumed circular shape (red) and elliptical shape (blue) for the ring and cyclone. Lower panel method assumes the perimeters are curves of constant \hat{T}_1 .

highly elliptical, so that the elliptical perimeter appears to better estimate the ring's true location. In contrast, the cyclone is much more circular, so that either perimeter adequately describes the cyclone's location.

The fourth method assumes that both the ring and cyclone perimeters are curves of constant $\hat{\Upsilon}_1$. For the ring, the value of $\hat{\Upsilon}_1$ is chosen as the value at the maximum azimuthal velocity point along a section directed northward from the ring's center (Figure 6, point A). For the cyclone, $\hat{\Upsilon}_1$ is chosen as the value at the maximum azimuthal velocity point along a section directed southward from the cyclone's center (Figure 6, point C). Note that the estimated perimeter location along these two sections is the same as that defined in the second method.

One hundred radial sections were equally spaced around the azimuth of each feature, and the radius to the specified $\hat{\Upsilon}_1$ was determined numerically along each section. The resulting estimated perimeter consists of 100 irregularly spaced points for each feature. The lower panel of Figure 10 shows the estimated ring and cyclone perimeters, overlaying the upper layer velocity field, for this method. As before, the ring and cyclone centers are shown as diamonds. These estimated perimeters have several distinct advantages over the previous estimates. First, all perimeter points for each feature lie within the modon boundary, so that no discontinuities in potential vorticity exist inside either feature. Second, the shape of each estimated perimeter closely matches the structure of the velocity field, especially for the ring, where the estimated perimeter is kidney-shaped, like the velocity distribution. Third, all points located on these estimated perimeters will remain on the perimeters as the solution evolves in time, since $\hat{\Upsilon}_1$ is globally conserved, as discussed previously. As a result, these perimeters will simply rotate along with the velocity field over time, *without change of shape*. Particle velocities on $\hat{\Upsilon}_1$ isolines are not constant, however, so that some contraction or expansion of particle spacing does occur over time. In addition, it should be emphasized that *no particles cross* the perimeters when they are defined

using this method.

In summary, four different methods were used to estimate ring and cyclone perimeters. The first three methods relied on the structure of the upper layer velocity field to define each feature's perimeter. The last method used the upper layer $\hat{\Upsilon}_1$ field to locate each perimeter. This method, in which each perimeter is defined as a curve of constant $\hat{\Upsilon}_1$, is the most satisfying. It arises naturally from the dynamics of the modon model and results in estimated perimeters that have several desirable characteristics.

5.2.3 Upper Layer Energetics

In the upper layer, APE and KE were calculated using (26), for both the ring and the entire layer, based on the method of Olson *et al.* (1985). APE is the fraction of total potential energy that is available to be converted to KE. Model energy estimates were made assuming three different forms for the ring's perimeter: circular, elliptical, and a curve of constant $\hat{\Upsilon}_1$, as discussed in the previous section and shown in Figure 10. Estimates of ring APE (KE), assuming a circular or elliptical ring, were within 8% (22%) of the estimate based on a perimeter of constant $\hat{\Upsilon}_1$. Since all energy estimates were comparable, only the estimates derived from assuming the ring perimeter as a curve of constant $\hat{\Upsilon}_1$ (Figure 10, lower panel) will be discussed here.

The estimates of ring APE and KE for WCR 82B made by Olson *et al.* (1985) were calculated using a diagnostic reduced gravity model. The authors point out that, because the model's lower layer was at rest, their ring energy estimates do not include the effects of uncompensated barotropic motions. They also stated that their estimated ring KE may be less accurate than the estimated ring APE since KE is more sensitive to contributions from the uncompensated barotropic modes. In contrast, the modon model has two active layers, so that estimates of ring energy reflect the contribution of the lower layer to both APE and KE. A comparison of ring

energy estimates from this simulation with the values reported by Olson *et al.* (1985) may provide some insight into the effects of lower layer motions on ring energetics.

If the ring's perimeter is assumed to be a curve of constant \hat{T}_1 , it's estimated APE is 5.1×10^{15} J, and it's estimated KE is 2.0×10^{14} J. The lower panel of Figure 4 shows that for this simulation ($\hat{r}_2 = 130$ km), assuming an elliptical ring results in an estimated APE of 4.7×10^{15} J and an estimated KE of 2.4×10^{14} J.

Olson *et al.* (1985) estimated a ring APE of about 4.1×10^{15} J and a ring KE of about 9.0×10^{14} J for the month of April, 1982. Agreement between the model ring APE and the Olson *et al.* (1985) estimate represents one independent assessment of the quality of this simulation. The ratio of simulated ring APE to APE estimated by Olson *et al.* (1985) is 1.24. The ratio of simulated ring KE to the Olson *et al.* (1985) estimate is 0.22. From this comparison, it seems likely that the estimated ring KE reported by Olson *et al.* (1985) may be an overestimate by as much as a factor of four.

When the entire upper layer is considered, the model's total APE is 1.7×10^{16} J, and the total KE is 9.8×10^{14} J. These values are 3.6 and 4.1 times the ring values, respectively. Based on this simulation, the dipole system contains roughly four times as much energy as the ring, when it is considered as an isolated feature.

5.2.4 Upper Layer Volume Transport

In the upper layer, along any north-south section, in Cartesian coordinates, volume transport \bar{V} may be expressed as

$$\bar{V} = \int_{y_a}^{y_b} u_1 H_1 dy \quad (27)$$

where u_1 is east-west velocity, H_1 is the undisturbed upper layer thickness (777 m for this simulation), and y_a and y_b are the south and north boundaries of the section.

For the ring system, peak volume transport occurs through a section along the line of centers, in the region between the ring and the cyclone, but exterior to both. If the ring and cyclone perimeters are assumed to be curves of constant \hat{T}_1 (Figure 10, lower panel), this region extends northward along the line of centers, from the northern edge of the cyclone (6 km north of the origin) to the southern edge of the ring (32 km north of the origin). This is a high velocity region, 26 km wide, with a great deal of water being "pumped" through it. From (27), \bar{V} for this section was evaluated numerically to be $1.25 \times 10^7 \text{ m}^3 \text{ s}^{-1}$, or 12.5 Sv ($1 \text{ Sv} = 10^6 \text{ m}^3 \text{ s}^{-1}$), directed to the west.

It is not clear how much of the transport between the ring and cyclone is due to recirculating water. Also, it is difficult to understand how \bar{V} varies as the dipole rotates. To better understand how the presence of the dipole might affect transport at the shelf break over time, a time series of \bar{V} was calculated along a north-south section, 150 km long, located 100 km to the west of the dipole center, over one modon rotation period. This section approximates the location of the MAB shelf-slope front as the WCR 82B system moved southwestward along the shelf slope.

The upper panel of Figure 11 shows the physical situation for this \bar{V} calculation at time zero. The ring and cyclone perimeters are assumed to be curves of constant \hat{T}_1 (shown in blue), and the north-south section representing the MAB shelf-slope front is shown in red. Contours of ψ_1 are also shown, with the contour interval in $\text{m}^2 \text{ s}^{-1}$ shown at the lower right. The lower panel of Figure 11 shows a time series of \bar{V} , in $\text{m}^3 \text{ km}^{-1} \text{ m}^{-1} \text{ s}^{-1}$, over one modon rotation period. Positive \bar{V} values represent transport directed to the east. This choice of units for \bar{V} allows transport to be expressed in $\text{m}^3 \text{ s}^{-1}$ per kilometer of shelf per meter depth, to allow for comparison with other transport estimates.

For comparison, Joyce *et al.* (1992) estimated a volume transport of 0.86 Sv through a 30 km section for an entrainment of shelf water by WCR 82B in June 1982. This transport estimate includes only water with salinity $\leq 35 \text{ ‰}$, representative of

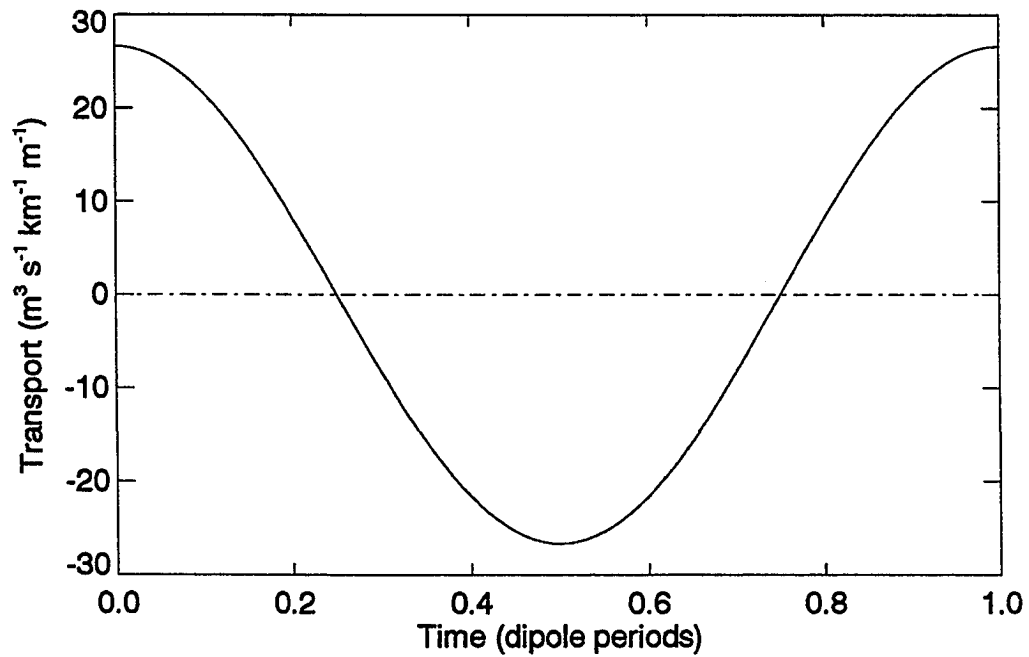
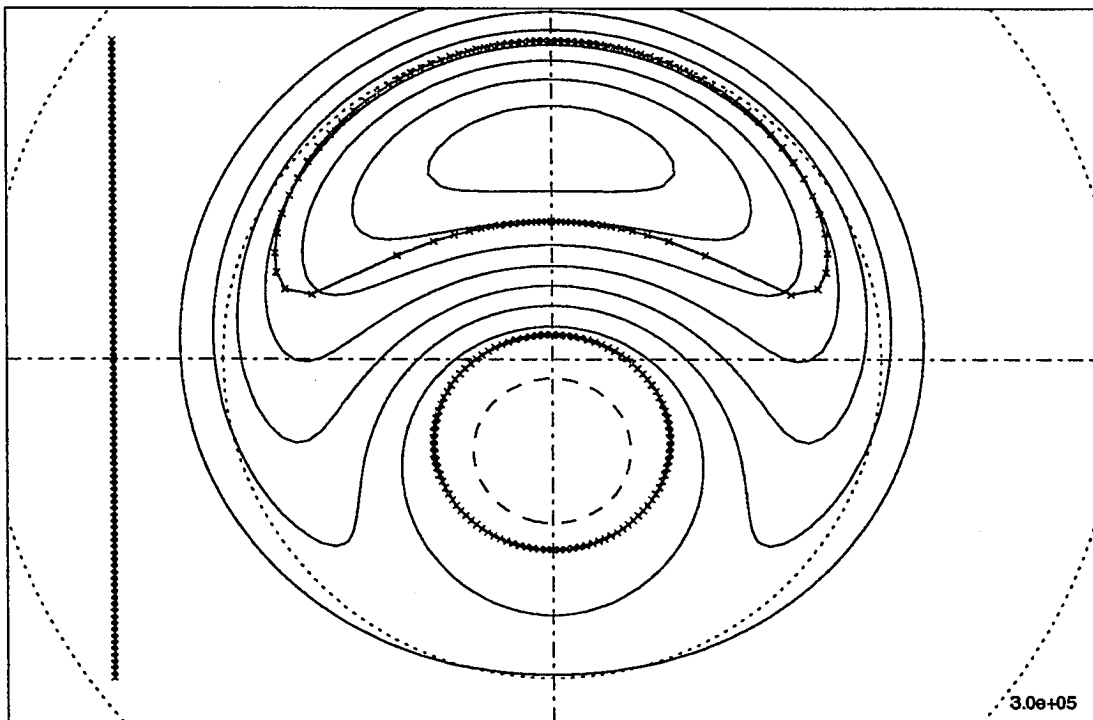


Figure 11: Volume transport through a section representing the MAB shelf-slope front. Upper panel shows ring and cyclone perimeters (blue) and a the MAB shelf-slope front section (red). Lower panel shows a time series of \bar{V} (in $\text{m}^3 \text{s}^{-1} \text{km}^{-1} \text{m}^{-1}$) through the section over one dipole rotation period.

shelf water. The average depth of this entrainment, estimated from Figure 3 in Joyce *et al.* (1992), is about 100 m. Although the section was *not* oriented north–south near the shelf break, this observation is consistent with other transport estimates for shelf water entrainment by WCR’s.

If the peak model transport of $26.6 \text{ m}^3 \text{ km}^{-1} \text{ m}^{-1} \text{ s}^{-1}$ from Figure 11 (lower panel) is used to calculate the equivalent transport through a 30 km long section of 100 m depth (a section similar to that made by Joyce *et al.*, 1992), the estimated transport is 0.08 Sv, about one–tenth of the transport observed by Joyce *et al.* (1992). However, the model transport was calculated over a 150 km long section, while the observations made by Joyce *et al.* (1992) spanned only 30 km. It is certainly possible to select shorter sections representative of the MAB shelf–slope front that would yield peak transports that agree more closely with the Joyce *et al.* (1992) measurement, but both the length and location of these sections would be arbitrary. The 150 km section used for this calculation should be viewed as representative of the entire dipole “footprint” along the MAB slope.

5.2.5 Lower Layer Kinematics

The upper panel of Figure 12 shows contours of the lower layer streamfunction ($\hat{\psi}_2$) field. Here, the field’s mean value has been subtracted for plot clarity, and the contour interval, in $\text{m}^2 \text{ s}^{-1}$, is shown in the lower right corner. The dot–dash axes show the location of the origin of the circular coordinate system. Dotted circles, with radii of 75 km and 130 km, show the upper and lower layer modon boundaries, respectively. The lower panel of Figure 12 shows the velocity vector map for the lower layer. Again, dot–dash axes show the location of the origin, and dotted circles show the modon boundaries. A 0.50 m s^{-1} velocity vector, shown at the upper right, provides a measure of velocity scale. Figure 12 shows that a large cyclone, centered at the origin, dominates the flow in the lower layer.

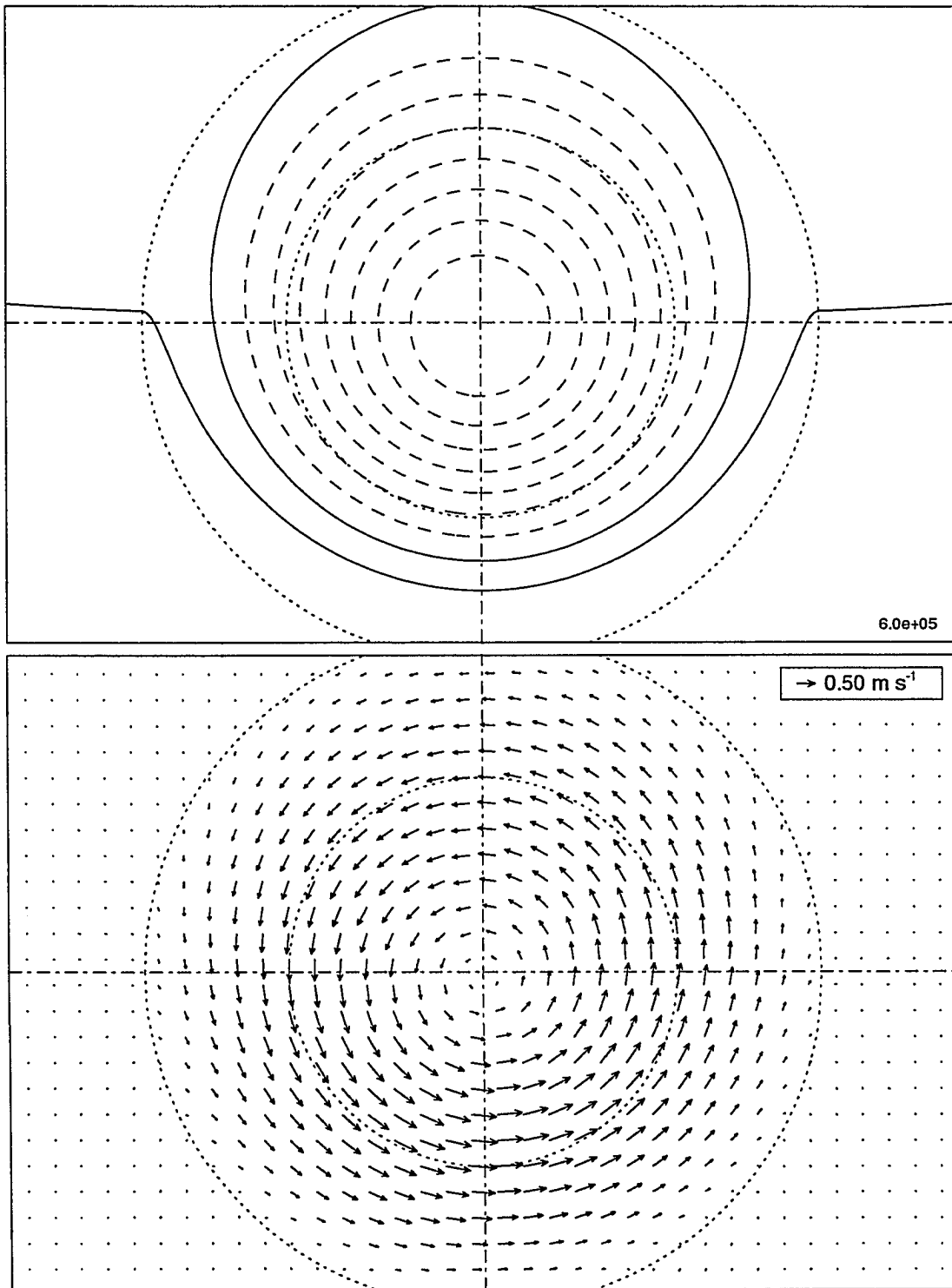


Figure 12: Contours of $\hat{\psi}_2$ field (upper panel) and lower layer velocity vectors (lower panel) for the diagnostic calculation.

Very little is known about the velocity structure of the deep layer below the WCR 82B system. However, Joyce (1984) reported results of hydrographic and velocity surveys of WCR 81D conducted in September 1981 as it approached the MAB after detaching from the Gulf Stream in July, 1981. No direct measurements of deep layer currents were made, but observations of shallow currents, combined with the gradient-current relationship, were used to infer deep layer velocities. Although difficulties with the procedure limited its accuracy, inferred deep layer velocities suggest that a cyclonic feature, comparable in size to WCR 81D, existed below the ring.

Since so little information about the deep ocean structure of the WCR 82B system is available, no lower layer observations were used to constrain the model parameters. Remember that the lower layer rider amplitude Ψ_2 was chosen so that the orbit rate ω of the cyclone around the ring's center matched the estimated value reported by Hooker and Brown (1994). The large cyclone present in the model's lower layer is therefore quite significant. It is consistent with the picture of deep ocean velocity structure below a WCR reported by Joyce (1984), and it arises naturally in a modon simulation when the model's parameters are constrained only by observations from the *upper* layer.

The lower layer cyclonic flow is also clearly evident in contour plots of potential vorticity \hat{q}_2 and effective streamfunction $\hat{\Upsilon}_2$. The upper panel in Figure 13 shows contours of \hat{q}_2 , as defined in (2b). The contour interval, in rad s^{-1} , is shown in the lower right corner. The lower panel in Figure 13 shows contours of $\hat{\Upsilon}_2$, as defined in (7). The contour interval, in $\text{m}^2 \text{s}^{-1}$, is shown in the lower right corner.

5.3 Results of the Evolutionary Calculations

The diagnostic calculation for this simulation provides some insight into the kinematic behavior of the model solution. However, it is difficult to predict the trajectories of fluid parcels from the diagnostic results because the solution fields are rotating

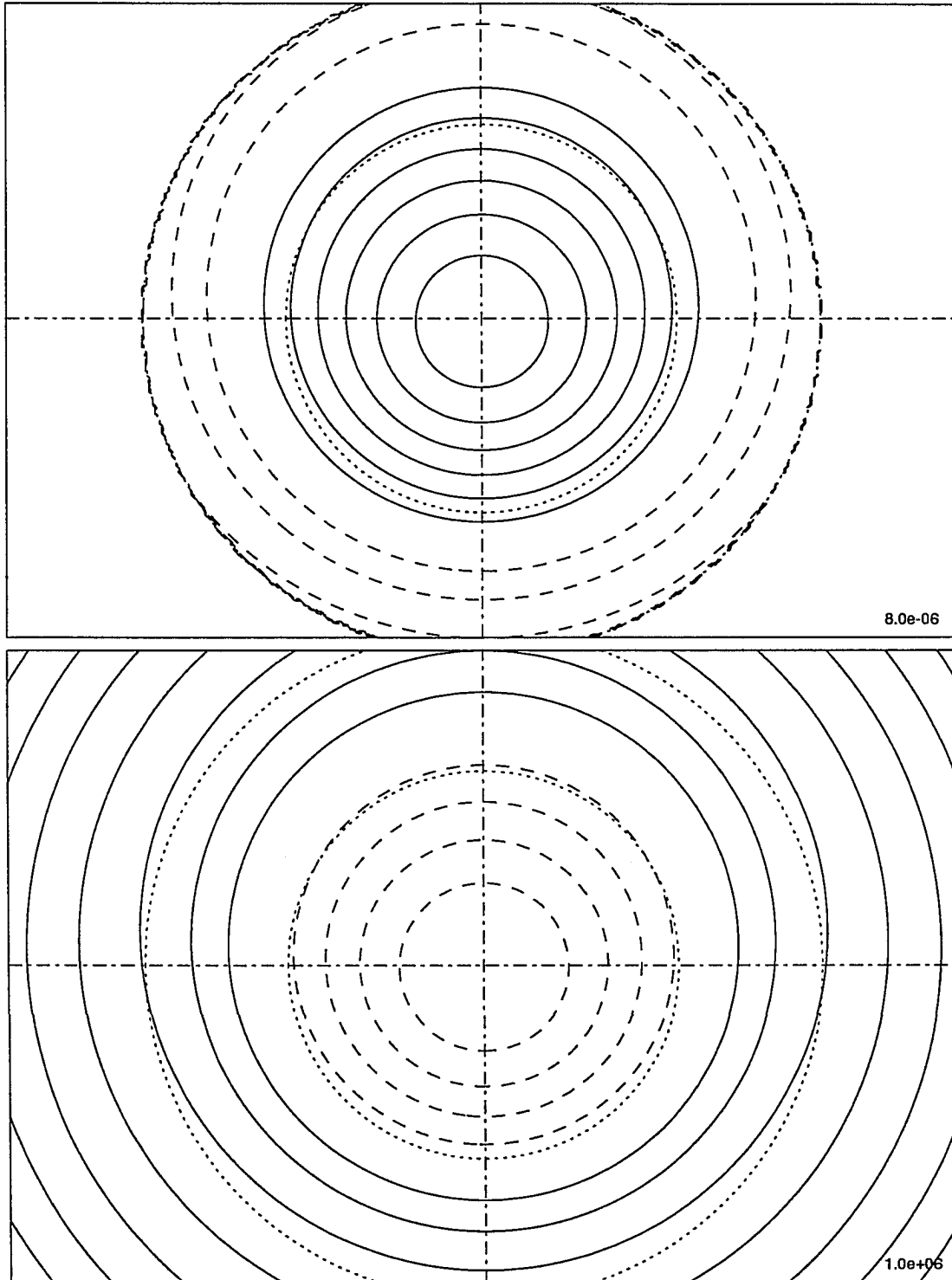


Figure 13: Contours of q_2 (upper panel) and Y_2 (lower panel) for the diagnostic calculation.

steadily in an anticyclonic sense. Since the streamfunction fields are time dependent, fluid parcels do *not* simply follow streamlines. The kinematic behavior of the simulated dipole becomes much clearer when fluid parcels are tracked as they evolve according to the time-dependent modon equations.

Fluid parcel trajectories are determined by integrating velocity equations with respect to time. In the circular coordinate system, velocity can be expressed nondimensionally as

$$\frac{dr_i}{dt} = -\frac{1}{r_i} \frac{\partial \psi_i}{\partial \theta_i}$$

$$\frac{d\theta_i}{dt} = \frac{1}{r_i} \frac{\partial \psi_i}{\partial r_i}$$

where i indicates the appropriate layer ($i = 1, 2$). For the evolutionary calculations, these equations were integrated numerically using a predictor-corrector scheme.

Two evolutionary calculations were performed. In the first calculation, three flow features that are apparent in a 24 April 1982 satellite image of surface temperature for the WCR 82B system were simulated by allowing the model to evolve over a 14-day period. Each flow feature was simulated as a separate fluid patch consisting of 2000 individual fluid parcels. The first patch, a rectangle 100 km long and 7 km wide with regularly spaced fluid parcels, oriented north-south, was initially located to the west of the dipole, representing a strip of MAB shelf water. The second patch was a circle of randomly placed parcels with a radius of 10 km. This patch was initially placed inside the cyclone. The third patch was also a 10 km radius circle of randomly placed parcels and was initially placed inside the ring.

For the first calculation, the simulated dipole was initially oriented with the ring to the east, and the cyclone to the west of the modon center. The three patches were allowed to evolve for a period of 14 days. The initial condition for this calculation is

shown in the upper panel of Figure 14, where each patch's initial position is overlaid on the $\hat{\psi}_1$ field at time zero. The contour interval for the $\hat{\psi}_1$ field is shown in the lower right corner. The first patch, the strip of MAB shelf water, is shown in red. The blue circular patch is located inside the cyclone. The green circular patch is located inside the ring.

The second calculation examined the evolution of two long, thin rectangular fluid patches that represent MAB shelf water (to the northwest of the dipole) and Gulf Stream water (to the southeast of the dipole). Each fluid patch consisted of 2500 regularly spaced fluid parcels, and they were allowed to evolve for a period of 7.4 days. The time period was chosen arbitrarily, serving only to demonstrate the model's ability to qualitatively reproduce observed flow features. At time zero, the simulated dipole was oriented with the ring to the southwest, and the cyclone to the northeast. This orientation is representative of the situation when the cyclone regains its circular shape after passing between the ring and the shelf break, as discussed by Hooker and Brown (1994).

The initial condition for this calculation is shown in the lower panel of Figure 14, where the initial position of both fluid patches is overlaid on the $\hat{\psi}_1$ field at time zero. The contour interval for the $\hat{\psi}_1$ field is shown in the lower right corner. Each patch is 12 km wide, consisting of five lines of parcels, with 3 km between lines. A single parcel line consists of 500 parcels, located at 0.7 km intervals along the line, so that each line is nearly 350 km long. MAB shelf water is represented by the patch located to the northwest, with parcel colors ranging from green to yellow moving away from the dipole. Gulf Stream water is represented by the patch to the southeast, with parcel colors ranging from red to blue moving away from the dipole.

The upper panel of Figure 15 shows a satellite image of sea surface temperature for 24 April 1982. The image shows WCR 82B, the large elliptical structure with a bright green core, near the center of the image, and an associated peripheral cyclone

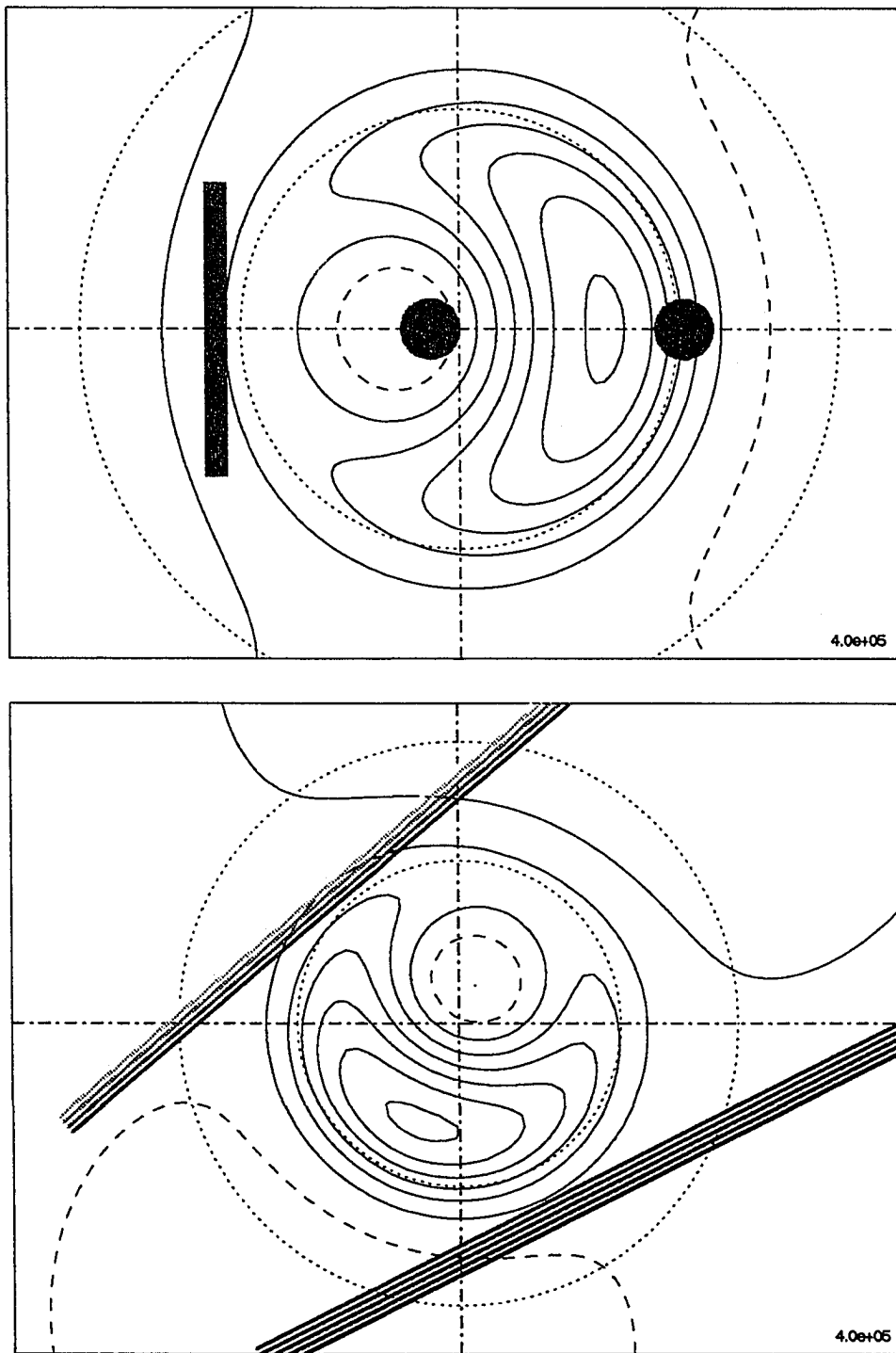


Figure 14: Initial conditions for the first (upper panel) and second (lower panel) evolutionary calculations. Each panel shows fluid patches overlaid on the $\hat{\psi}_1$ field at time zero.

located southeast along the ring's perimeter, shown as a banded grey feature with a dark core. The data shown in the image has not been enhanced in any way, but a hybrid zebra color palette, described by Hooker and Brown (1994), has been used to provide distinct boundaries between temperature regimes. These dark boundaries clearly indicate the sense of rotation of each feature shown in the image.

The first calculation simulates three flow features, apparent in this image, as individual fluid patches. The first feature to be simulated is the large, curved filament (dark grey) surrounding the northern periphery of the ring and extending as a straight line between the ring and cyclone. South of the ring and cyclone, a pool of fluid collects at the tail of the filament. This feature will be simulated by the red fluid strip of MAB shelf water initially positioned as shown in Figure 14 (upper panel). The second feature to be simulated is the blackish comma shape seen in the center of the cyclone with a tail extending down to the southwest. This feature is simulated by the blue initially circular patch of cyclone water (Figure 14, upper panel). The green wispy inward spiral in the center of the ring (Figure 15, upper panel) is the third feature to be simulated. The green circular patch, initially positioned as shown in Figure 14 (upper panel), will represent this spiral.

The initial positions of the fluid patches are somewhat arbitrary, and were chosen only to reproduce the desired flow features in the simplest way. The initial orientation of the dipole and the integration time of 14 days are also arbitrary, and were chosen simply to demonstrate that the model is capable of producing the kinds of flow features seen in the imagery.

The lower panel of Figure 15 shows the final distribution of parcels for the three patches after 14 days. The red strip was entrained by the ring as it moved through its anticyclonic rotation, and was deformed into a long thin filament encircling the ring's perimeter and extending through the region between the ring and cyclone. Many red fluid parcels were "pumped" through the region between the ring and the

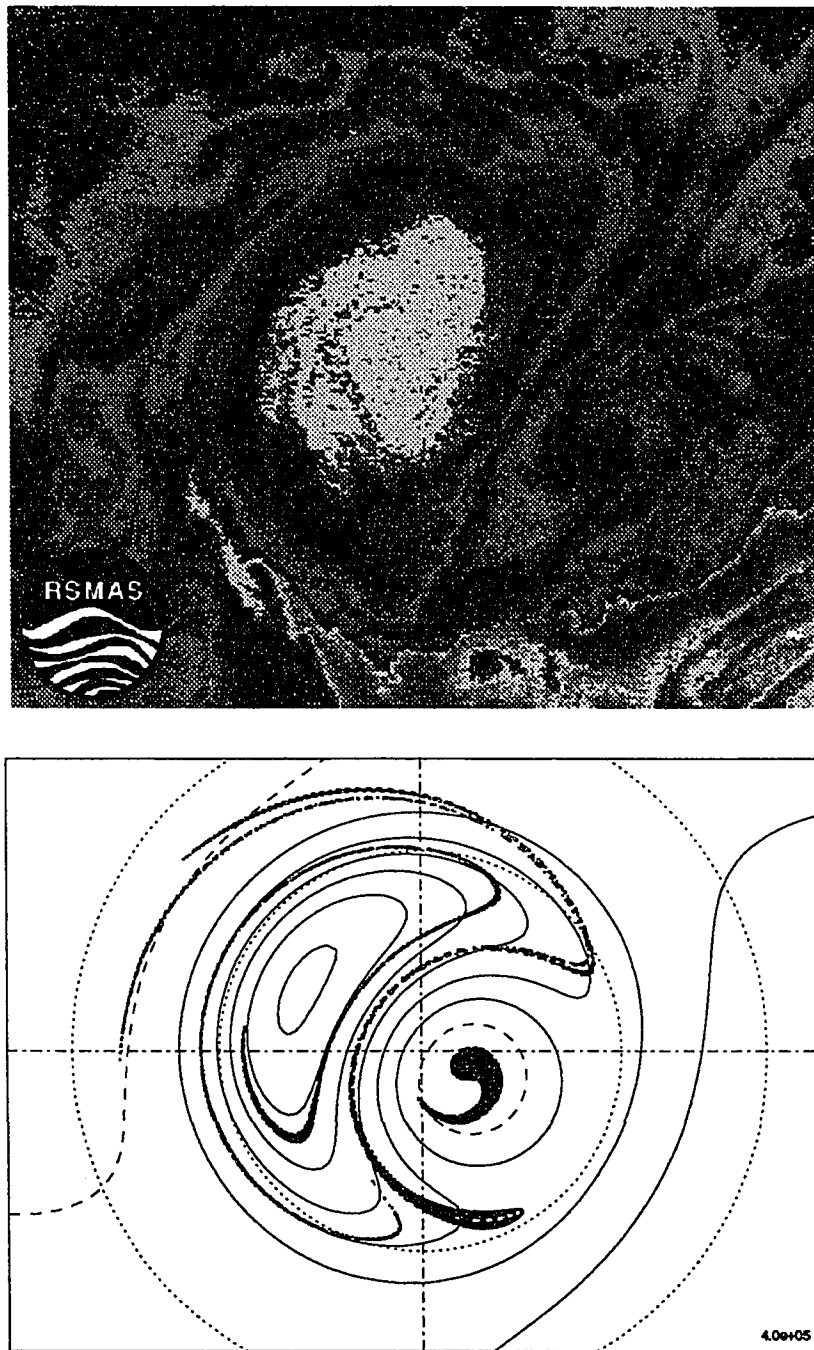


Figure 15: Comparison of 24 April 1982 surface temperature image (upper panel) with parcel distributions from the first evolutionary calculation (with three fluid patches), after 14 days (lower panel).

cyclone, and a “pool” of red parcels is collecting just south of the cyclone. This pool of water at the filament’s tail is similar to what is seen in the image (upper panel). The distribution of parcels between the ring and cyclone is much more curved in the simulation, however.

Figure 15 (lower panel) shows that the initially circular blue patch of cyclone water is deformed into a distinctive comma shape after 14 days, with all blue parcels remaining trapped inside the cyclone. This comma shape is very similar to the structure of the cyclone’s core seen in the image (upper panel). This comma shaped structure shows that, in the cyclone’s interior, fluid spirals inward toward the cyclone center. This spiral structure is remarkable since the model permits no horizontal convergence/divergence.

Another inward spiral develops in the ring’s interior after 14 days. Figure 15 (lower panel) shows that the green circle of ring water has been stretched into a string of parcels showing a clear inward spiral toward the ring’s center. All green fluid parcels remain in the ring’s interior. A wispy trace of an inward spiral inside the ring is apparent in the image (upper panel). This spiral, too, is remarkable since no convergence/divergence occurs in the model.

The upper panel of Figure 16 shows a sea surface temperature image for 23 April 1982. This image covers a larger area than the image shown in Figure 15, and it includes the dipolar structure of the WCR 82B system, as well as adjacent MAB shelf water and Gulf Stream water, to allow for comparison with the results of the patch evolution calculation. The same hybrid zebra color palette used for the image in Figure 15 was also used for this image. The ring is again shown as a large elliptical structure with a bright green core, and the cyclone is again located southeast of the ring along its perimeter. MAB shelf water is shown as the deep blue (cooler) region to the northwest, and Gulf Stream water is shown as the yellow and orange (warmer) water located in the southeast corner of the image.

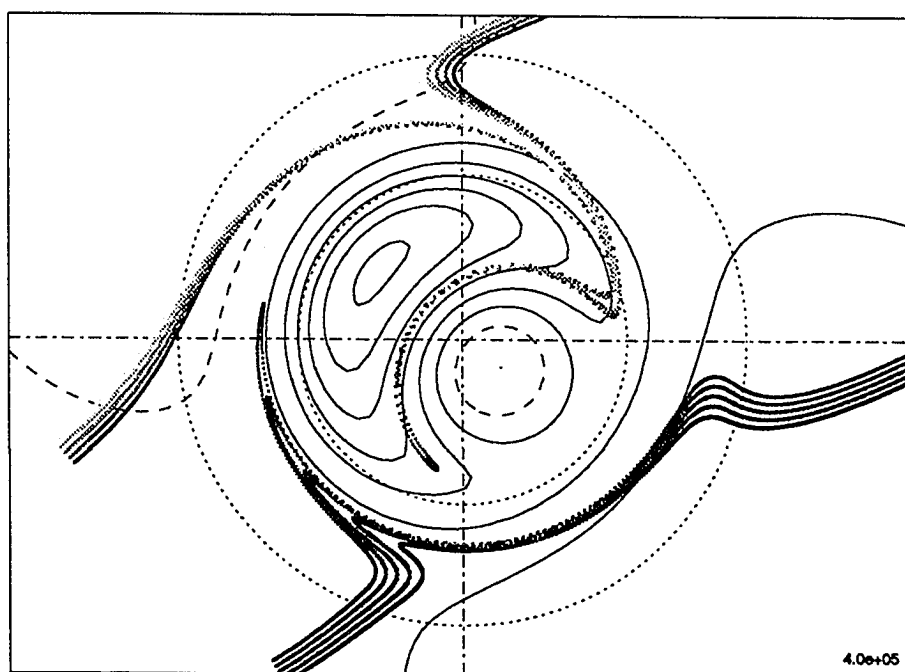


Figure 16: Comparison of 23 April 1982 surface temperature image (upper panel) with parcel distributions from the second evolutionary calculation (simulating MAB shelf and Gulf Stream water masses), after 7.4 days (lower panel).

The lower panel of Figure 16 shows the final distribution of parcels for the second calculation, after 7.4 days. This calculation was constructed to simulate the flow field shown in the upper panel image. Look first at the MAB shelf patch located to the northwest. This patch was initially located along the boundary of the MAB shelf-slope region, as shown in Figure 14 (lower panel). After 7.4 days, the ring, initially located to the south, has moved anticyclonically to the northwest, passing near the MAB fluid patch. The lower panel of Figure 16 shows that the ring has entrained a significant number of parcels from this patch, and they are now spread around more than half of the ring's perimeter. Many parcels have been "pumped" through the region between the ring and cyclone. The grey filament encircling the ring in the image (Figure 16, upper panel) shows a similar distribution extending completely through the region between the ring and cyclone. Note that simulated parcels located in the region between the ring and cyclone have a very curved distribution, compared to a straight, almost linear, structure shown in the image.

Now look at the Gulf Stream patch located to the southeast. The upper panel of Figure 16 shows a tongue of Gulf Stream water (yellow) extending up to the northwest and beginning to wrap around the ring, near the center of the image. The lower panel of Figure 16 shows that the simulated Gulf Stream patch has developed a very similar tongue after 7.4 days. In addition, the small "bump" of yellow Gulf Stream water located immediately to the southeast of the cyclone (Figure 16, upper panel) is also apparent in the simulated field after 7.4 days (lower panel). This bump is apparently an indication of flow beginning to wrap around the cyclone's perimeter as it rotates adjacent to the Gulf Stream.

The results of the two evolutionary calculations show that the modon model simulation of the WCR 82B system can reproduce many features of the surface flow field apparent in satellite imagery. Results from the first calculation indicate that a single surface temperature image may contain information about the surface flow field

covering time spans of at least 14 days.

6 Discussion and Conclusions

6.1 Limitations of the Modon Model

The purpose of this work was to simulate the WCR 82B system, consisting of WCR 82B and one peripheral cyclone, as a rotating baroclinic modon, and to evaluate the simulation by comparing model results with observations. Additionally, the model was used to calculate some quantities not directly measured for this system (ring energies, volume transport, and lower layer flow), and these model results were compared to estimates based on observations. Energies for the dipole system were also calculated. Finally, the modon simulation was used to calculate the location of the ring and cyclone perimeters by four different methods.

The modon model is a two-layer, flat-bottom QG model with a steadily rotating analytic solution form. Because of its relative simplicity, application of the model to the simulation of the WCR 82B system has several limitations. First, the model is QG and cannot account for ageostrophic motions, which may be important, particularly in energetic mesoscale features like ring systems. Note, however, that the radius to maximum azimuthal velocity for both the ring (56 km, Figure 7, upper right panel) and the cyclone (31 km, Figure 8, upper right panel) are larger than the simulated dipole's internal deformation radius (26.4 km, section 4), so that adequate resolution of the dipole's flow structure should be expected. However, as stated at the outset, this simulation is viewed simply as a "first step" toward more complete understanding dipole dynamics.

Second, the simulated dipole exists over a flat bottom, while the WCR 82B system was observed to move southwestward along the MAB slope, as shown in Figure 1 of

Evans *et al.* (1985). Careful examination of the track of WCR 82B, however, shows that its center remained near the 2700 m isobath throughout the simulation period, with its perimeter spanning depths from 2300 m to about 3000 m. The ring, then, did not “ride up” onto the slope, but appeared to be “steered” by the bottom topography, with the total depth variation below the ring limited to 25% or less of the depth at ring center. While the presence of a sloping bottom below WCR 82B certainly plays a role in the system’s dynamics, it appears that the bottom topography may act as a steering mechanism for a translating ring system *already in vorticity balance* rather than as a vorticity source/sink for a ring interacting dynamically with steep topography.

There is observational evidence suggesting that bottom topography is *not* an important factor in dipole dynamics, so that a flat-bottom modon model is useful for initial ring system studies. Joyce (1984) observed a small cyclone northeast of WCR 81D, which was located east of the New England Seamounts, a region with relatively flat bottom and water depths exceeding 4500 m. Also, dipole structures, either cyclones orbiting WCR’s or anticyclones orbiting CCR’s, have recently been noted in analysis of satellite surface temperature imagery (S. Hooker, personal communication). Many of these dipole structures are seen to exist in deep water, over a flat bottom.

Third, the modon model is local, with no horizontal boundaries, so that interactions of the simulated dipole with the adjacent MAB shelf, the Gulf Stream, or other ring systems, cannot be addressed. As noted above, the WCR 82B system moved along an isobath on the MAB slope. Dynamical effects of the MAB slope might best be addressed, then, by the inclusion of a wall boundary. Since the modon model has no horizontal boundaries, the simulation cannot account for wall effects. Hooker and Brown (1994) use a point vortex model to study how a dipole is affected by an adjacent wall. Their results show that the presence of the wall causes the peripheral

cyclone to elongate into a filament as it is advected through the gap between the ring and the boundary. The cyclone emerges on the far side of the gap and eventually reforms. Interactions with the boundary result in periodic cycles of cyclone filamentation and reformation.

Fourth, the model cannot account for dipole translation. Estimates of translation speeds for WCR 82B range from 9 km d^{-1} (Hooker and Olson, 1984) to 13 km d^{-1} (Joyce and Kennelly, 1984) for June, 1982. A rotating, translating, baroclinic modon solution currently does not exist (although it may eventually be found), so that the modon modeler must choose *either* translation *or* rotation in building a simulation of this type. While translation is clearly an important dynamical process, this simulation necessarily includes only rotation effects.

Fifth, the model has no mechanism for decay or “spin-down” of the ring system. Numerous observations show that ring systems gradually spin down over their lifetime, becoming generally smaller and weaker with time. The model, however, includes no dissipation processes, so that spindown effects cannot be simulated in evolutionary calculations. However, the longest time period covered by evolutionary calculations presented here is 14 days, a time span too short for dissipation effects to be important. The consideration of spin-down processes is left for future research.

In addition to the model limitations discussed above, it should be noted that the stability of the baroclinic modon solution in a primitive equation environment has not been studied in detail. Lipphardt *et al.* (1994) reported preliminary results for studies using a rotating *barotropic* modon solution as an initial condition for a two-layer primitive equation simulation over a flat bottom. They observed that the cyclone and anticyclone rapidly redistribute their internal relative vorticity and ultimately undergo mutual advection. Additional studies must be done to address the stability of the baroclinic solution.

6.2 Discussion of Results

The baroclinic modon simulation of the WCR 82B system produced two sets of results. First, the diagnostic calculation examined the characteristics of the solution (velocity structure, energies, volume transport) at a fixed time, and allowed for four different estimates of the location of the ring and cyclone perimeters. Second, two calculations were constructed to simulate several flow features seen in satellite imagery by observing changes in the distribution of fluid patches as the model evolved over time.

The diagnostic calculation showed that, in the upper layer, the ring's velocity structure was kidney-shaped, while the cyclone was much more circular. This flow-field geometry is inherent in the modon model since the entire dipole is confined to a circular region defined by \hat{r}_1 . If the dipole is symmetric (peak ring and cyclone vorticities are equal in magnitude), then both the ring and cyclone exhibit semi-circular flow structure. As the ring strength increases relative to the cyclone, the ring deforms into the kidney shape, and the cyclone becomes more circular. It is not clear from observations of the velocity structure of the WCR 82B system how well the simulated flow geometry represents the true flow field.

Of the four methods used to estimate the location of the ring and cyclone perimeters, the one which assumes the perimeters to be $\hat{\Upsilon}_1$ isolines provides the best results. This estimated perimeter arises naturally from the model's dynamics, and describes a curve that does not change shape as the dipole evolves. Additionally, no fluid parcels cross a perimeter defined using this method, so that the perimeter exactly encloses a region of "recirculating" water in the ring and cyclone interiors.

There is some uncertainty in the exact value of $\hat{\Upsilon}_1$ chosen to define each perimeter for this method. The perimeters shown in Figure 10 (lower panel) were located using the $\hat{\Upsilon}_1$ value corresponding to the maximum azimuthal velocity points along the line of centers (Figure 6, points A and C). A similar definition for other radii relative

to each feature's center will yield slightly different \hat{T}_1 values. To provide a useful perimeter estimate, the value of \hat{T}_1 that is chosen need only correspond to a closed curve.

In principle, the technique presented here for estimating the location of the ring and cyclone perimeters could be applied to observations of other dipole systems. Here, however, information about the ring and cyclone velocity structure, estimates of stratification, and an estimated ω , were all required to properly constrain the model. Application to other systems will require some way to estimate these quantities.

Ring and dipole energies were calculated from the results of the diagnostic calculation. Ring APE was consistent with an estimate derived from a reduced-gravity model, but ring KE was one-fourth of the reduced-gravity model estimate. Energy estimates for the dipole system were approximately four times higher than those for the ring. This suggests that multipole ring systems may be much more important than isolated rings in oceanic energy budgets. This result motivates a need for detailed census information about multipole ring systems.

For a realistic value of entrainment depth, the simulated dipole was shown to pump 1.6 Sv of water through a 26 km wide region between the ring and cyclone. If this pumped flow is directed across the shelf, a dipole located at the shelf edge (like the WCR 82B system for much of its life) could be an important mechanism for driving brief, intense periods of cross-shelf transport. This is another important result motivating a need for a detailed census of these multipole systems.

Although very little is known about the deep ocean structure associated with ring systems, this simulation suggests that a large cyclone may exist under this type of rotating dipole, consistent with the preliminary findings of Joyce (1984). Future observations of deep ocean velocity structure are needed to determine if this result is typical of other dipole ring systems.

The two evolutionary calculations demonstrate that, in addition to producing

a simulated dipole with kinematic characteristics similar to the observed system, evolving fluid patches from the model can reproduce many features of the surface flow inferred from satellite surface temperature imagery. The model dipole can account for entrainment of MAB shelf water, ultimately pumping the entrained water between the ring and cyclone. The model also accounts for inward spiraling of interior ring and cyclone water in a region with no convergence. The model dipole, when located between the MAB shelf break and the Gulf Stream, entrains both MAB shelf water and Gulf Stream water, similar to the flow inferred from imagery.

Fluid pumped between the ring and cyclone shows a much more curved distribution in the model (red parcels in the lower panel of Figure 15), when compared to the satellite image (Figure 15, upper panel). The curved distribution in the model results from the asymmetry of the dipole (the ring's peak vorticity is higher than that of the cyclone). If the dipole is made more symmetric, by increasing the value of b_{+n}^I , parcels moving between the ring and cyclone will follow straighter paths, more like those seen in the image. Increasing the value of b_{+n}^I , however, generally results in higher velocities for both the ring and cyclone, so that the simulation's error index E , as defined in (25), increases, indicating that the simulated dipole's kinematic characteristics deviate farther from their observed values. The chosen values for the observed quantities, as discussed in section 4.5, were based on azimuthally averaged velocity profiles, however. It is likely that an alternate set of observed values with higher ring and cyclone velocities will result in a higher b_{+n}^I and a straighter distribution of parcels between the ring and cyclone. Alternate choices for observed values of ring and cyclone velocities should be constrained by the limits of the data scatter shown in the left hand panels of Figures 7 and 8. Identifying alternate values for the observed velocities was not attempted here.

6.3 Conclusions

Several conclusions can be made from this application of the baroclinic modon model to the simulation of the WCR 82B system:

- When observed ring and cyclone velocity profiles, combined with estimates of center-to-center distance and cyclone orbit rate, are used to constrain the baroclinic modon model parameters, the model produces a steadily rotating dipole. The simulated ring and cyclone velocities are comparable to the azimuthally averaged observed values.
- Dipolar modon solutions in which the ring peak vorticity is higher than the cyclone peak vorticity result in ring velocity structures that are somewhat kidney-shaped. The cyclone velocity structure is more circular in these cases.
- When the WCR 82B system is assumed to be a dipole, baroclinic modon dynamics produces a simulated ring with APE comparable to the estimated APE from a reduced gravity model for the ring. The KE of the ring from the modon model (which includes effects of a dynamically active lower layer) is roughly one-fourth of the estimate from the reduced gravity model. The ring's KE, then, may be significantly lower than was previously thought.
- Based on the baroclinic modon simulation of the WCR 82B system, dipole ring systems, consisting of a WCR paired with a cyclone, can contain roughly four times as much energy (both APE and KE) as an isolated ring. Since multipole structures have been observed for both WCR's and CCR's, this simulation motivates a reevaluation of the importance of ring *systems* in the ocean's energy balance.
- In the upper layer (777 m), the simulated dipole pumps more than 12 Sv of water through a region 26 km wide, between the ring and the cyclone. For a

150 km long section representing the MAB shelf-slope front, the peak dipole transport is $26.6 \text{ m}^3 \text{ s}^{-1}$ per kilometer of shelf per meter depth. Model transport was about one-tenth of the observed transport for one entrainment by WCR 82B. Dipole systems like this may be an important mechanism for brief, intense shelf-slope transport.

- The baroclinic modon simulation of the WCR 82B system suggests that the deep ocean structure below the dipole consists of a large cyclone that spans the region below both the ring and the peripheral cyclone.
- Baroclinic modon dynamics produce a simulated dipole that accounts for many flow features apparent in surface temperature imagery of the WCR 82B system. The simulated dipole entrains shelf water and pumps it between the ring and cyclone, and interior water in both the ring and cyclone evolves into inward spirals, even though no convergence occurs. The simulated dipole also entrains both MAB shelf water and Gulf Stream water when it is located between the MAB shelf edge and the eastward Gulf Stream boundary.
- Baroclinic modon dynamics are insufficient to describe dipole translation, spin-down processes, and interactions with wall boundaries. In addition, some flow features observable in the satellite imagery, like the scalloping that occurs at edge of the MAB shelf water entrainment along the ring's periphery (Figure 15, upper panel), cannot be produced with the model.

6.4 What's the Next Step?

This study represents the first effort to apply baroclinic modon dynamics to the simulation of a multipole ring system. The results are encouraging, and they suggest several possibilities for future research:

- Perhaps a better method can be found for constraining the modon model param-

eters using additional information from the observations. In particular, since the simulated ring and cyclone velocity fields are clearly not axisymmetric, constraining the model based on azimuthally averaged velocity information may not be appropriate.

- The difficulties encountered in constraining the model parameters for this simulation reveal a need for more detailed velocity measurements of ring systems. Although detailed surveys of rings are cost prohibitive, future observational programs must focus on rings as part of multipole vortex systems, rather than simply as isolated features. Velocity surveys must be constructed to allow for the possible existence of peripheral flow features.
- This study represents one application of baroclinic modon dynamics to a single observed ring system. Although detailed velocity information is usually not available, satellite surface temperature imagery, combined with some assumptions about the underlying velocity structure, may provide enough information to allow for a baroclinic modon simulation of other systems. A simulation like this could provide useful information about system energies, lower layer structure, and perimeter locations for the features.
- Because multipole ring systems may play a prominent role in ocean energy budgets and cross-shelf transport, details about their location and frequency of occurrence are needed. This could be accomplished through careful analysis of satellite images of both WCR and CCR systems. The resulting census of multipole rings could be combined with these simulation results to yield a revised estimate of the energy contained in mesoscale ring systems.
- As discussed above, the baroclinic modon solution needs to be tested for stability. Using the solution to initialize a primitive equation model would provide insight into how the solution behaves when ageostrophic responses are permit-

ted. Also, the stability of the perturbed solution might be addressed using a numerical solution scheme to solve a perturbed form of the baroclinic modon equations.

- The baroclinic modon model represents an autonomous system of five nonlinear equations. When viewed from the dynamical systems perspective, it represents a unique opportunity to examine a geophysical fluid dynamics system for chaotic properties. These simulation results should provide some motivation, since they demonstrate the model's applicability to mesoscale ring systems, which are observed to occur frequently in nature.

References

- Allen, J. S., R. C. Beardsley, J. O. Blanton, W. C. Boicourt, B. Butman, L. K. Coachman, A. Huyer, T. H. Kinder, T. C. Royer, J. D. Schumacher, R. L. Smith, W. Sturges, and C. D. Winant. Physical oceanography of continental shelves. *Rev. of Geophys. Space Phys.*, 21:1149–1181, 1983.
- Beardsley, R. C. and W. C. Boicourt. On estuarine and continental-shelf circulation in the Middle Atlantic Bight. In B. A. Warren and W. C., editors, *Evolution of Physical Oceanography*, pages 198–233. MIT Press, 1981.
- Beardsley, R. C., W. C. Boicourt, and D. V. Hansen. Physical oceanography of the Middle Atlantic Bight. In M. G. Gross, editor, *Middle Atlantic Continental Shelf and the New York Bight*, pages 20–34. Amer. Soc. Limnol. Oceanogr., Special Symposia, 2, 1976.
- Beardsley, R. C., D. C. Chapman, K. H. Brink, S. R. Ramp, and R. Schlitz. The Nantucket Shoals Flux Experiment (NSFE 79). Part I: A basic description of the current and temperature variability. *J. Phys. Oceanogr.*, 15:713–758, 1985.
- Bisagni, J. J. Lagrangian current measurements within the eastern margin of a warm-core Gulf Stream ring. *J. Phys. Oceanogr.*, 13:709–715, 1983.
- Brink, K. H. Coastal ocean physical processes. *Rev. of Geophys.*, 25:204–216, 1987.
- Brown, O. B., P. C. Cornillon, S. R. Emmerson, and H. M. Carle. Gulf Stream warm rings: A statistical study of their behavior. *Deep Sea Res.*, 33:1459–1473, 1986.
- Bumpus, D. F. A description of the circulation on the continental shelf of the east coast of the United States. *Prog. Oceanogr.*, 6:111–157, 1973.
- Chapman, D. C., J. A. Barth, and R. C. Beardsley. On the continuity of mean flow between the Scotian Shelf and the Middle Atlantic Bight. *J. Phys. Oceanogr.*, 16:758–772, 1986.
- Chapman, D. C. and R. C. Beardsley. On the origin of shelf water in the Middle Atlantic Bight. *J. Phys. Oceanogr.*, 19:384–391, 1989.
- Churchill, J. H., P. C. Cornillon, and G. W. Milkowski. A cyclonic eddy and shelf-slope water exchange associated with a Gulf Stream warm-core ring. *J. Geophys. Res.*, 91:9615–9623, 1986.
- Cushman-Roisin, B., W. H. Heil, and D. Nof. Oscillations and rotations of elliptical warm-core rings. *J. Geophys. Res.*, 90:11756–11764, 1985.
- Emery, W. J., W. G. Lee, and L. Magaard. Geographic and seasonal distributions of Brunt-Väisälä frequency and Rossby radii in the North Pacific and North Atlantic. *J. Phys. Oceanogr.*, 14:294–317, 1984.
- Evans, R. H., K. S. Baker, O. B. Brown, and R. C. Smith. Chronology of warm-core ring 82B. *J. Geophys. Res.*, 90:8803–8811, 1985.

- Fairbanks, R. G. The origin of continental shelf and slope water in the New York Bight and the Gulf of Maine: Evidence from $H_2^{18}O/H_2^{16}O$ ratio measurements. *J. Geophys. Res.*, 87:5796–5808, 1982.
- Fischer, H. B. Mixing processes on the Atlantic continental shelf, Cape Cod to Cape Hatteras. *Limnol. Oceanogr.*, 25:114–125, 1980.
- Flierl, G. R. A simple model for the structure of warm and cold core rings. *J. Geophys. Res.*, 84:781–785, 1979.
- Flierl, G. R., V. D. Larichev, J. C. McWilliams, and G. M. Reznik. The dynamics of baroclinic and barotropic solitary eddies. *Dyn. Atmos. Oceans.*, 5:1–41, 1980.
- Flierl, G. R., M. E. Stern, and J. A. Whitehead. The physical significance of modons: Laboratory experiments and general integral constraints. *Dyn. Atmos. Oceans.*, 7:233–263, 1983.
- Fornshell, J. A. and W. A. Criess. Anticyclonic eddy observations in the slope water aboard CGC Evergreen. *J. Phys. Oceanogr.*, 9:992–1000, 1979.
- Garvine, R. W., K. C. Wong, and G. G. Gawarkiewicz. The morphology of shelfbreak eddies. *J. Geophys. Res.*, 93:15593–15607, 1988.
- Gotthardt, G. A. and G. J. Potocsky. Life cycle of a Gulf Stream anticyclonic eddy observed from several oceanographic platforms. *J. Phys. Oceanogr.*, 4:131–134, 1974.
- Halliwell, G. R., Jr. and C. N. K. Mooers. The space-time structure and variability of the shelf water-slope water and Gulf Stream surface temperature fronts and associated warm-core eddies. *J. Geophys. Res.*, 84:7707–7725, 1979.
- Hooker, S. B. and J. W. Brown. Warm core ring dynamics derived from satellite imagery. *J. Geophys. Res.*, 99:25181–25194, 1994.
- Hooker, S. B. and D. B. Olson. Center of mass estimation in closed vortices: A verification in principle and practice. *J. Atmos. Oceanic Technol.*, 1:247–255, 1984.
- Houghton, R. W. and J. Marra. Physical/biological structure and exchange across the thermohaline shelf/slope front in the New York Bight. *J. Geophys. Res.*, 88:4467–4481, 1983.
- Houghton, R. W., D. B. Olson, and P. J. Celone. Observation of an anticyclonic eddy near the continental shelf break south of New England. *J. Phys. Oceanogr.*, 16:60–71, 1986.
- Joyce, T. M. Velocity and hydrographic structure of a Gulf Stream warm-core ring. *J. Phys. Oceanogr.*, 14:936–947, 1984.
- Joyce, T. M. Gulf Stream warm-core ring collection: An introduction. *J. Geophys. Res.*, 90:8801–8802, 1985.
- Joyce, T. M., J. K. B. Bishop, and O. B. Brown. Observations of offshore shelf-water transport induced by a warm-core ring. *Deep Sea Res.*, 39:S97–S113, 1992.

- Joyce, T. M. and M. A. Kennelly. Upper-ocean velocity structure of Gulf Stream warm-core ring 82B. *J. Geophys. Res.*, 90:8839-8844, 1985.
- Kennelly, M. A., R. H. Evans, and T. M. Joyce. Small-scale cyclones on the periphery of a Gulf Stream warm-core ring. *J. Geophys. Res.*, 90:8845-8857, 1985.
- Ketchum, B. H. and D. J. Keen. The accumulation of river water over the continental shelf between Cape Cod and Chesapeake Bay. *Deep Sea Res.*, 3 (suppl.):346-357, 1955.
- Kirwan, A. D., Jr., R. P. Mied, and B. L. Lipphardt, Jr. Rotating modons over isolated topography in a stratified ocean. *Dyn. Atmos. Oceans*. (submitted), 1995.
- Kirwan, A. D., Jr., W. J. Merrell, Jr., J. K. Lewis, R. E. Whitaker, and R. Legeckis. A model for the analysis of drifter data with an application to a warm-core ring in the Gulf of Mexico. *J. Geophys. Res.*, 89:3425-3438, 1984.
- Lai, D. Y. and P. L. Richardson. Distribution and movement of Gulf Stream rings. *J. Phys. Oceanogr.*, 7:670-683, 1977.
- Larichev, V. D. and G. M. Reznik. Two dimensional Rossby soliton: An exact solution. *Polymode News*, 19, 1976.
- Lipphardt, B. L., Jr., R. P. Mied, A. D. Kirwan, Jr., and G. J. Lindemann. Evolution of a rotating barotropic modon in a primitive equation model. In G. J. F. van Heijst, editor, *Modelling of Oceanic Vortices*, pages 259-269. Royal Netherlands Academy of Arts and Sciences, 1994.
- McWilliams, J. C. and G. R. Flierl. On the evolution of isolated, nonlinear vortices. *J. Phys. Oceanogr.*, 9:1155-1182, 1979.
- Mied, R. P., A. D. Kirwan, Jr., and G. J. Lindemann. Rotating modons over isolated topographic features. *J. Phys. Oceanogr.*, 22:1569-1582, 1992.
- Mied, R. P. and G. J. Lindemann. The propagation and evolution of cyclonic Gulf Stream rings. *J. Phys. Oceanogr.*, 9:1183-1205, 1979.
- Mied, R. P. and G. J. Lindemann. The birth and evolution of eastward-propagating modons. *J. Phys. Oceanogr.*, 12:213-230, 1982.
- Mooers, C. N. K., R. W. Garvine, and W. W. Martin. Summertime synoptic variability of the Middle Atlantic shelf water/slope water front. *J. Geophys. Res.*, 84:4837-4854, 1979.
- Morgan, C. W. and J. M. Bishop. An example of Gulf Stream eddy-induced water exchange in the Mid-Atlantic Bight. *J. Phys. Oceanogr.*, 7:472-479, 1977.
- Nof, D. On the β -induced movement of isolated baroclinic eddies. *J. Phys. Oceanogr.*, 11:1662-1672, 1981.
- Nof, D. On the ellipticity of isolated anticyclonic eddies. *Tellus*, 37A:77-86, 1985.

- Olson, D. B., R. W. Schmitt, M. Kennelly, and T. M. Joyce. A two-layer diagnostic model of the long-term physical evolution of warm-core ring 82B. *J. Geophys. Res.*, 90:8813-8822, 1985.
- Ramp, S. R., R. C. Beardsley, and R. Legeckis. An observation of frontal wave development on a shelf-slope/warm core ring front near the shelf break south of New England. *J. Phys. Oceanogr.*, 13:907-912, 1983.
- Richardson, P. L. Gulf Stream rings. In A. R. Robinson, editor, *Eddies in Marine Science*, pages 19-45. Springer-Verlag, 1983.
- Richardson, P. L., R. E. Cheney, and L. V. Worthington. A census of Gulf Stream rings, spring 1975. *J. Geophys. Res.*, 83:6136-6144, 1978.
- Saunders, P. M. Anticyclonic eddies formed from shoreward meanders of the Gulf Stream. *Deep Sea Res.*, 18:1207-1219, 1971.
- Smith, D. C. IV and J. J. O'Brien. The interaction of a two-layer isolated mesoscale eddy with bottom topography. *J. Phys. Oceanogr.*, 13:1681-1697, 1983.
- Smith, P. C. Low-frequency fluxes of momentum, heat, salt, and nutrients at the edge of the Scotian Shelf. *J. Geophys. Res.*, 83:4079-4096, 1978.
- Stern, M. E. Minimal properties of planetary eddies. *J. Mar. Res.*, 33:1-13, 1975.
- Voorhis, A. D., D. C. Webb, and R. C. Millard. Current structure and mixing in the shelf/slope water front south of New England. *J. Geophys. Res.*, 81:3695-3708, 1976.
- Wang, X. W. *Interaction of an eddy with a continental slope*. PhD thesis, MIT-WHOI Joint Program in Oceanography, 1992.
- Wright, W. R. The limits of shelf water south of Cape Cod, 1941 to 1972. *J. Mar. Res.*, 34:1-14, 1976.

Curriculum Vitae

Bruce L. Lipphardt, Jr.

Date of Birth: July 25, 1962

Place of Birth: Cleveland, Ohio

Education

1995	Ph.D.	Oceanography	Old Dominion University
1984	B.S.	Oceanography	U. S. Naval Academy (with distinction)

Awards and Honors

Trident Scholar, U. S. Naval Academy, 1983–1984

National Defense Science and Engineering Graduate Fellowship, 1990–1993

Honorary and Professional Affiliations

Phi Kappa Phi	American Meteorological Society
Sigma Xi	The Oceanography Society
American Geophysical Union	Mathematical Association of America

Refereed Publications

“Rotating modons over isolated topography in a stratified ocean” *Dyn. Atmos. Oceans* (submitted), 1995. (with A. D. Kirwan, Jr. and R. P. Mied)

“Nonlinear ocean dynamics.” In *The Oceans: Physical–Chemical Dynamics and Human Impact*, edited by S. K. Majumdar, E. W. Miller, G. S. Forbes, R. F. Schmalz and A. A. Panah, pp. 40–55, The Pennsylvania Academy of Science, 1994. (with A. D. Kirwan, Jr. and K. L. Gregory)

“Coherent flows with near zero potential vorticity.” *J. Mar. Sys.*, 4, 95–115, 1993. (with A. D. Kirwan, Jr.)

“Negative potential vorticity lenses.” *Int. J. Engng. Sci.*, 30, 1361–1378, 1992. (with A. D. Kirwan, Jr. and J. Liu)

Other Publications

“Evolution of a rotating barotropic modon in a primitive equation model.” In *Modeling of oceanic vortices*, edited by G. J. F. van Heijst, pp. 259–269, Royal Netherlands Academy of Arts and Sciences, 1994. (with R. P. Mied, A. D. Kirwan, Jr., and G. J. Lindemann)

“Hydrographic data collected aboard RV Nathaniel B. Palmer, March–May 1993.” *CCPO Technical Report No. 93-04*, 215 pp., Center for Coastal Physical Oceanography, Old Dominion University, Norfolk, Virginia, 1993. (with D. A. Smith, R. A. Locarnini and E. E. Hofmann)

“XBT data collected aboard RV Nathaniel B. Palmer, March–May 1993.” *CCPO Technical Report No. 93-06*, 158 pp., Center for Coastal Physical Oceanography,

Old Dominion University, Norfolk, Virginia, 1993. (with D. A. Smith, R. A. Locarnini and E. E. Hofmann)

"Palmer LTER: Hydrography in the LTER region." *Ant. J. of the U. S.*, 28, 209-211, 1993. (with E. Hofmann, R. A. Locarnini, and D. A. Smith)

"Variations with time of the carbon dioxide partial pressure in central and south Atlantic surface waters." *U. S. Naval Academy Trident Scholar Report 130*, 1984.